INSTITUTE OF PHYSICS PUBLISHING INVERSE PROBLEMS

Inverse Problems **18** (2002) 1733–1759 PII: S0266-5611(02)38334-5

Linear and nonlinear inversion algorithms applied in nondestructive evaluation

R Marklein[1], **K Mayer**[1], **R Hannemann**[1], **T Krylow**[1], **K Balasubramanian**[1], **K J Langenberg**[1] **and V Schmitz**[2]

[1] Electromagnetic Theory, Department of Electrical Engineering/Computer Science, University of Kassel, D-34109 Kassel, Germany
[2] Fraunhofer-Institute for Nondestructive Testing, University of the Saarland, D-66123 Saarbrücken, Germany

E-mail: marklein@uni-kassel.de and langenberg@uni-kassel.de

Received 18 June 2002, in final form 12 August 2002
Published 8 November 2002
Online at stacks.iop.org/IP/18/1733

Abstract

Convenient tools for nondestructive evaluation of solids can be electromagnetic and/or elastodynamic waves; since their governing equations, including acoustics, exhibit strong structural similarities, the same inversion concepts apply. In particular, the heuristic SAFT algorithm (synthetic aperture focusing technique) can be—and has been—utilized for all kinds of waves, once a scalar approximation can be justified. Relating SAFT to inverse scattering in terms of diffraction tomography, it turns out that linearization is the most stringent inherent approximation. Hence, the results of nonlinear inversion schemes such as contrast source inversion are compared to the output of SAFT for a carefully designed ultrasonic experiment. In addition, it will be shown via synthetic as well as experimental data that SAFT can be extended to electromagnetic vector fields and to an inhomogeneous and/or anisotropic background material.

(Some figures in this article are in colour only in the electronic version)

1. Introduction

Historically, imaging in nondestructive evaluation started with the utilization of ultrasonic waves (in solids) adopting the radar imaging concept SAR (synthetic aperture radar) under the acronym of SAFT (synthetic aperture focusing technique) (Fitch 1988, Ganapathy *et al* 1982). SAFT is understood as a synthetic focusing of time domain wavefronts emanating from an ensemble of point scatterers back to their (secondary, equivalent, induced) sources for homogeneous isotropic lossless media and scalar (acoustic) waves; in terms of time domain backpropagation this is simply based on the knowledge of the infinite-space scalar Green function. To date, SAFT has been evaluated as a powerful tool in nondestructive testing

with ultrasound (Müller and Schmitz 2002), where the transition from acoustic (fluid) to solid media has been made by applying appropriate time gating techniques between primary (P- or pressure) and secondary (S- or shear) waves. For practical applications the aim is towards a fast automated three-dimensional implementation; on the other hand, improvements and extensions of the SAFT algorithm require that we address more fundamental issues:

- embedding in the theory of wavefield inversion resulting in a connection with frequency domain diffraction tomography (Langenberg 1987, 2002, Langenberg *et al* 1993b, 1997, 1999b) and a pertinent implementation based on Fourier transforms only (FT-SAFT: Mayer 1990, Mayer *et al* 1990),
- utilization of polarization when applied to electromagnetic waves (Langenberg *et al* 1994, 1999a, Brandfaß 1996),
- utilization of mode conversion for elastodynamic waves in solids (Langenberg *et al* 2002) and formulating backpropagation for inhomogeneous anisotropic media (Langenberg *et al* 1997, Hannemann 2002),
- complementing SAFT with nonlinear inverse scattering schemes (Marklein *et al* 2001),
- combination with numerical modelling techniques to obtain a convenient test bed for various versions of the algorithm (Langenberg *et al* 1993b, 1999b, 2002, Marklein 1997).

These itemized issues are addressed in this paper and supported by actual examples.

Regarding mathematical notation, vectors and tensors are written with boldface characters, the number of underlines indicating the rank, i.e. a vector with one underline appears as a tensor of rank one.

Regarding engineering notation, a (multi-)monostatic or pulse–echo experiment collects data with the same 'antenna' used as transmitter and receiver, whereas a (multi-)bistatic or pitch–catch experiment collects data for separated transmitting and receiving 'antennas'; here, 'multi' refers to a scan within a finite-measurement aperture of the transmitting–receiving or the receiving 'antenna'.

2. Wavefield inversion

Scattering of wavefields can be physically understood and mathematically formulated as a radiation of equivalent, secondary or induced sources in terms of Huygens' principle as a consequence of the underlying governing equations. This requires knowledge of the Green functions!

Figures 1–3 introduce the governing equations Fourier transformed with regard to time ($e^{j\omega t}$ as kernel of the Fourier transform) of acoustics, electromagnetics and elastodynamics together with the pertinent integral representations of the respective wavefields as given by prescribed (volume) sources (de Hoop 1995). Since we confine ourselves to linear time-invariant materials, the Fourier transform is a convenient tool to switch between the time and frequency domains; this is often appropriate for mathematical derivations, even though a deliberately chosen space may be more advantageous for algorithmic implementation.

Linear time-invariant homogeneous isotropic instantaneously and locally reacting acoustic media are characterized by two scalar material constants, ρ, the mass density, and κ, the (adiabatic) compressibility. Then, the field quantities $\underline{\boldsymbol{v}}(\underline{\boldsymbol{R}}, \omega)$ (Fourier transform of the particle velocity with respect to time) and $p(\underline{\boldsymbol{R}}, \omega)$ (Fourier transform of the pressure), both depending on the vector of position $\underline{\boldsymbol{R}}$ and the Fourier variable (circular frequency) ω, are related by the governing equations of acoustics, as given in the middle of figure 1: particles are accelerated by a pressure gradient and external forces (Fourier transform of force density $\underline{\boldsymbol{f}}(\underline{\boldsymbol{R}}, \omega)$), and the divergence of a particle flow together with an external (Fourier transformed) dilatation

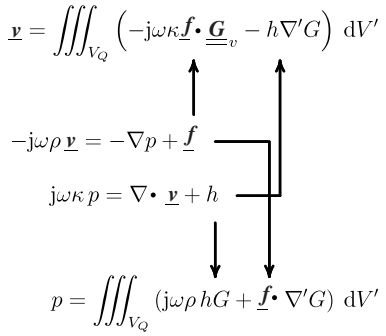

Figure 1. Green functions relating to the acoustic volume sources of force density $\underline{\boldsymbol{f}}$ and dilatation rate h.

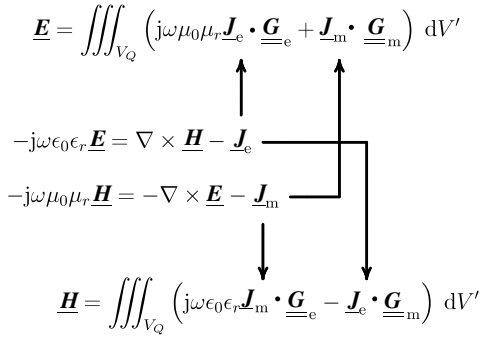

Figure 2. Green functions relating to the electromagnetic volume sources of electric and magnetic current densities, $\underline{\boldsymbol{J}}_\mathrm{e}$ and $\underline{\boldsymbol{J}}_\mathrm{m}$, respectively.

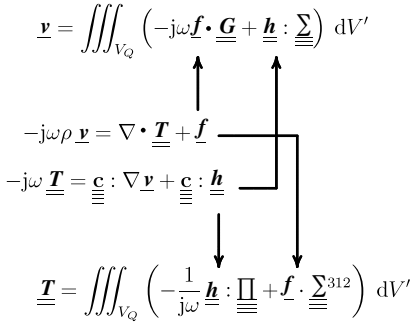

Figure 3. Green functions relating to the elastodynamic volume sources of force density $\underline{\boldsymbol{f}}$ and (symmetric) injected deformation rate $\underline{\underline{\boldsymbol{h}}}$; $\underline{\underline{\underline{\mathbf{c}}}}$ is the stiffness tensor for homogeneous isotropic lossless media.

rate $h(\underline{\boldsymbol{R}}, \omega)$ cause a rate of change of the pressure. Introducing infinite-space Green function Fourier spectra

$$G(\underline{\boldsymbol{R}} - \underline{\boldsymbol{R}}', \omega) = \frac{\mathrm{e}^{\mathrm{j}k|\underline{\boldsymbol{R}} - \underline{\boldsymbol{R}}'|}}{4\pi\,|\underline{\boldsymbol{R}} - \underline{\boldsymbol{R}}'|}, \tag{1}$$

$$\underline{\underline{\boldsymbol{G}}}_v(\underline{\boldsymbol{R}} - \underline{\boldsymbol{R}}') = -\frac{1}{k^2}\nabla'\nabla' G(\underline{\boldsymbol{R}} - \underline{\boldsymbol{R}}', \omega), \qquad \underline{\boldsymbol{R}} \neq \underline{\boldsymbol{R}}', \tag{2}$$

with the wavenumber

$$k = \omega\sqrt{\kappa\rho}, \tag{3}$$

the field quantities are given by integral representations (figure 1, top and bottom) *outside* the source volume[1] V_Q to which the sources are considered to be confined. As soon as a scattering volume V_c is present besides the source volume V_Q, $\underline{\boldsymbol{v}}(\underline{\boldsymbol{R}}, \omega) \Longrightarrow \underline{\boldsymbol{v}}_i(\underline{\boldsymbol{R}}, \omega)$ and $p(\underline{\boldsymbol{R}}, \omega) \Longrightarrow p_i(\underline{\boldsymbol{R}}, \omega)$, as given in figure 1, can be interpreted as (prescribed) incident fields, which have to be complemented by scattered fields $\underline{\boldsymbol{v}}_s(\underline{\boldsymbol{R}}, \omega)$ and $p_s(\underline{\boldsymbol{R}}, \omega)$ to satisfy the transition (boundary) conditions for the total fields $\underline{\boldsymbol{v}} = \underline{\boldsymbol{v}}_i + \underline{\boldsymbol{v}}_s$, $p = p_i + p_s$ on S_c, the surface of V_c; this surface is conveniently described by its (vector) singular function $\underline{\gamma}_c(\underline{\boldsymbol{R}})$, which has the direction of the outward normal $\underline{\boldsymbol{n}}_c$ (Bleistein 1984, van Bladel 1996). Since we are looking for a Huygens-type representation of the scattered fields in terms of Helmholtz integrals *outside* V_c, the extinction theorem tells us that this representation must yield zero fields *inside* V_c; the transition conditions as obtained from the governing equations define surface force densities and surface dilatation rates

$$\underline{\boldsymbol{f}}_c(\underline{\boldsymbol{R}}, \omega) = p(\underline{\boldsymbol{R}}, \omega)\,\underline{\gamma}_c(\underline{\boldsymbol{R}}), \tag{4}$$

$$h_c(\underline{\boldsymbol{R}}, \omega) = -\underline{\boldsymbol{v}}(\underline{\boldsymbol{R}}, \omega) \cdot \underline{\gamma}_c(\underline{\boldsymbol{R}}), \tag{5}$$

which sustain the discontinuous jump from zero fields inside to the total fields outside.

When inserted into the integral representations of figure 1, we obtain, for instance, the Helmholtz integral for the scattered pressure (due to the sifting property of the singular function) for $\underline{\boldsymbol{R}}$ outside V_c:

$$p_s(\underline{\boldsymbol{R}}, \omega) = \int\!\!\int_{S_c} [-\mathrm{j}\omega\rho\underline{\boldsymbol{n}}'_c \cdot \underline{\boldsymbol{v}}(\underline{\boldsymbol{R}}', \omega)G(\underline{\boldsymbol{R}} - \underline{\boldsymbol{R}}', \omega) + p(\underline{\boldsymbol{R}}', \omega)\underline{\boldsymbol{n}}'_c \cdot \nabla' G(\underline{\boldsymbol{R}} - \underline{\boldsymbol{R}}', \omega)]\,\mathrm{d}S'. \tag{6}$$

Let us assume now that the scatterer is defined by a Dirichlet boundary condition, i.e. it is considered to be acoustically soft. Then (6) reduces to

$$p_s(\underline{\boldsymbol{R}}, \omega) = -\mathrm{j}\omega\rho \int\!\!\int_{S_c} \underline{\boldsymbol{n}}'_c \cdot \underline{\boldsymbol{v}}(\underline{\boldsymbol{R}}', \omega)G(\underline{\boldsymbol{R}} - \underline{\boldsymbol{R}}', \omega)\,\mathrm{d}S'. \tag{7}$$

If $p_s(\underline{\boldsymbol{R}}, \omega)$ with $\underline{\boldsymbol{R}}$ on some measurement surface S_M is considered as data, inversion of (7) aims towards the equivalent sources on S_c: here, the normal component of the particle velocity or, via the first governing equation in figure 1, the normal derivative of the pressure. The first attempt to solve this inversion is—linearization! For a perfect scatterer like the acoustically soft scatterer the introduction of the Kirchhoff or physical optics (PO) approximation yields the required linearization in terms of

$$p_s^{\mathrm{PO}}(\underline{\boldsymbol{R}}, \omega) = -2\mathrm{j}\omega\rho \int\!\!\int_{S_c} \underline{\boldsymbol{n}}'_c \cdot \underline{\boldsymbol{v}}_i(\underline{\boldsymbol{R}}', \omega)G(\underline{\boldsymbol{R}} - \underline{\boldsymbol{R}}', \omega)u(-\hat{\underline{\boldsymbol{k}}}_i \cdot \underline{\boldsymbol{n}}'_c)\,\mathrm{d}S', \tag{8}$$

where the total field under the integral has been replaced by twice the incident field, and the unit step-function $u(-\hat{\underline{\boldsymbol{k}}}_i \cdot \underline{\boldsymbol{n}}'_c)$ accounts for the illuminated part of the scattering surface. Equation (8) is the key equation for diffraction tomography (Dändliker and Weiss 1970), and a particularly simple version is obtained for far-field data; in that case, the approximation

$$G^{\mathrm{far}}(\underline{\boldsymbol{R}}, \underline{\boldsymbol{R}}', \omega) = \frac{\mathrm{e}^{\mathrm{j}kR}}{4\pi R}\,\mathrm{e}^{-\mathrm{j}k\hat{\underline{\boldsymbol{R}}}\cdot\underline{\boldsymbol{R}}'} \tag{9}$$

[1] For observation points $\underline{\boldsymbol{R}}$ *inside* the source volume (integration is with respect to $\underline{\boldsymbol{R}}'$), $\underline{\underline{\boldsymbol{G}}}_v$ must be complemented by δ-distributional terms (de Hoop 1995, van Bladel 1996).

($\hat{\underline{\boldsymbol{R}}}$ is the unit vector to $\underline{\boldsymbol{R}}$) together with a plane wave ansatz

$$\underline{\boldsymbol{v}}_i(\underline{\boldsymbol{R}}, \omega) = \underline{\boldsymbol{v}}_0(\omega) \mathrm{e}^{\mathrm{j}k\hat{\underline{\boldsymbol{k}}}_i \cdot \underline{\boldsymbol{R}}} \tag{10}$$

with propagation direction $\hat{\underline{\boldsymbol{k}}}_i$ and longitudinal polarization $\underline{\boldsymbol{v}}_0(\omega)$ for the incident field basically turns (8) into a three-dimensional spatial Fourier integral with the Fourier vector

$$\underline{\boldsymbol{K}} = k(\hat{\underline{\boldsymbol{R}}} - \hat{\underline{\boldsymbol{k}}}_i) \tag{11}$$

provided an appropriate diversity experiment has been made, and, obviously, either frequency (ω) or angular diversity ($\hat{\underline{\boldsymbol{k}}}_i$) is available. Hence, in these cases, inversion is straightforward; details are given by Langenberg (2002).

Turning to electromagnetic wavefield inversion, the same fundamental ideas as above apply, but with an additional complexity: electromagnetic waves exhibit polarization diversity, which must be properly accounted for.

Figure 2 shows the time harmonic governing equations (Maxwell equations) for a linear time-invariant homogeneous isotropic instantaneously and locally reacting medium with relative permittivity ϵ_r and relative permeability μ_r. Field quantities in that case are the (Fourier transformed) electric field strength $\underline{\boldsymbol{E}}(\underline{\boldsymbol{R}}, \omega)$ and the (Fourier transformed) magnetic field strength $\underline{\boldsymbol{H}}(\underline{\boldsymbol{R}}, \omega)$, and given (field independent) sources are electric and magnetic current densities, $\underline{\boldsymbol{J}}_{\mathrm{e}}(\underline{\boldsymbol{R}}, \omega)$ and $\underline{\boldsymbol{J}}_{\mathrm{m}}(\underline{\boldsymbol{R}}, \omega)$, respectively.

Since both Maxwell equations exhibit the same spatial (curl) derivative (the origin of duality), the same Green functions ($\underline{\boldsymbol{R}} \neq \underline{\boldsymbol{R}}'$)

$$\underline{\underline{\boldsymbol{G}}}_{\mathrm{e}} = \left(\underline{\underline{\boldsymbol{I}}} + \frac{1}{k^2}\nabla'\nabla'\right) G(\underline{\boldsymbol{R}} - \underline{\boldsymbol{R}}', \omega), \tag{12}$$

$$\underline{\underline{\boldsymbol{G}}}_{\mathrm{m}} = -\nabla' \times \underline{\underline{\boldsymbol{G}}}_{\mathrm{e}}(\underline{\boldsymbol{R}} - \underline{\boldsymbol{R}}', \omega) = -\nabla' G(\underline{\boldsymbol{R}} - \underline{\boldsymbol{R}}', \omega) \times \underline{\underline{\boldsymbol{I}}} \tag{13}$$

appear in both volume source integrals in figure 2 ($\underline{\boldsymbol{R}} \notin V_Q$); $\underline{\underline{\boldsymbol{I}}}$ is the dyadic idem factor and

$$k = \omega\sqrt{\epsilon_0 \epsilon_r \mu_0 \mu_r} \tag{14}$$

the electromagnetic wavenumber. As in the acoustic case, the definition of field-dependent equivalent sources

$$\underline{\boldsymbol{J}}_{\mathrm{ec}}(\underline{\boldsymbol{R}}, \omega) = \underline{\gamma}_c(\underline{\boldsymbol{R}}) \times \underline{\boldsymbol{H}}(\underline{\boldsymbol{R}}, \omega), \tag{15}$$

$$\underline{\boldsymbol{J}}_{\mathrm{mc}}(\underline{\boldsymbol{R}}, \omega) = -\underline{\gamma}_c(\underline{\boldsymbol{R}}) \times \underline{\boldsymbol{E}}(\underline{\boldsymbol{R}}, \omega) \tag{16}$$

on S_c yields, for instance, the representation

$$\begin{aligned}\underline{\boldsymbol{E}}_s(\underline{\boldsymbol{R}}, \omega) = \iint_{S_c} [&\mathrm{j}\omega\mu_0\mu_r \underline{\boldsymbol{n}}'_c \times \underline{\boldsymbol{H}}(\underline{\boldsymbol{R}}', \omega) \cdot \underline{\underline{\boldsymbol{G}}}_{\mathrm{e}}(\underline{\boldsymbol{R}} - \underline{\boldsymbol{R}}', \omega) \\ &- \underline{\boldsymbol{n}}'_c \times \underline{\boldsymbol{E}}(\underline{\boldsymbol{R}}', \omega) \cdot \underline{\underline{\boldsymbol{G}}}_{\mathrm{m}}(\underline{\boldsymbol{R}} - \underline{\boldsymbol{R}}', \omega)] \, \mathrm{d}S'\end{aligned} \tag{17}$$

for the scattered electric field outside V_c. The special case of a perfect electric conductor V_c reduces (17) to

$$\underline{\boldsymbol{E}}_s(\underline{\boldsymbol{R}}, \omega) = \mathrm{j}\omega\mu_0\mu_r \iint_{S_c} \underline{\boldsymbol{n}}'_c \times \underline{\boldsymbol{H}}(\underline{\boldsymbol{R}}', \omega) \cdot \underline{\underline{\boldsymbol{G}}}_{\mathrm{e}}(\underline{\boldsymbol{R}} - \underline{\boldsymbol{R}}', \omega) \, \mathrm{d}S', \tag{18}$$

and within the far-field approximation

$$\underline{\underline{\boldsymbol{G}}}_{\mathrm{e}}^{\mathrm{far}}(\underline{\boldsymbol{R}}, \underline{\boldsymbol{R}}', \omega) = (\underline{\underline{\boldsymbol{I}}} - \hat{\underline{\boldsymbol{R}}}\,\hat{\underline{\boldsymbol{R}}}) G^{\mathrm{far}}(\underline{\boldsymbol{R}}, \underline{\boldsymbol{R}}', \omega) \tag{19}$$

we obtain

$$\underline{\boldsymbol{E}}_s^{\mathrm{far}}(\underline{\boldsymbol{R}}, \omega) = \mathrm{j}\omega\mu_0\mu_r \frac{\mathrm{e}^{\mathrm{j}kR}}{4\pi R} (\underline{\underline{\boldsymbol{I}}} - \hat{\underline{\boldsymbol{R}}}\,\hat{\underline{\boldsymbol{R}}}) \cdot \iint_{S_c} \underline{\boldsymbol{n}}'_c \times \underline{\boldsymbol{H}}(\underline{\boldsymbol{R}}', \omega) \, \mathrm{e}^{-\mathrm{j}k\hat{\underline{\boldsymbol{R}}} \cdot \underline{\boldsymbol{R}}'} \, \mathrm{d}S'. \tag{20}$$

Now, even though we are close to a Fourier inversion scheme after introducing the linearizing Kirchhoff approximation

$$\underline{\boldsymbol{J}}_{\mathrm{ec}}^{\mathrm{PO}}(\underline{\boldsymbol{R}},\omega) = 2\underline{\gamma}_u(\underline{\boldsymbol{R}}) \times \underline{\boldsymbol{H}}_i(\underline{\boldsymbol{R}},\omega) \tag{21}$$

with

$$\underline{\gamma}_u(\underline{\boldsymbol{R}}) = \underline{\gamma}_c(\underline{\boldsymbol{R}})u(-\underline{\hat{\boldsymbol{k}}}_i \cdot \underline{\boldsymbol{n}}_c) \tag{22}$$

we are not yet finished due to the zero determinant of the second-rank tensor $\underline{\underline{\boldsymbol{I}}} - \underline{\hat{\boldsymbol{R}}}\,\underline{\hat{\boldsymbol{R}}}$, i.e. it cannot be inverted in order to operate on the data $\underline{\boldsymbol{E}}_s^{\mathrm{far}}$ and not on the equivalent sources.

The elastodynamic governing equations can be picked from figure 3; following Cauchy, the scalar pressure has to be replaced by the second-rank (symmetric) stress tensor $\underline{\underline{\boldsymbol{T}}}(\underline{\boldsymbol{R}},\omega)$ (i.e. its Fourier transform), and the second equation is nothing but the definition of the dyadic deformation rate together with Hooke's law of linear elasticity for time-invariant homogeneous isotropic instantaneously and locally reacting media. Hence, the fourth-rank stiffness tensor $\underline{\underline{\underline{\underline{\boldsymbol{c}}}}}$ is understood to be composed of only two (Lamé) constants λ and μ:

$$\underline{\underline{\underline{\underline{\boldsymbol{c}}}}} = \lambda\,\underline{\underline{\underline{\underline{\boldsymbol{I}}}}}^{\delta} + 2\mu\,\underline{\underline{\underline{\underline{\boldsymbol{I}}}}}^{+}; \tag{23}$$

here, $\underline{\underline{\underline{\underline{\boldsymbol{I}}}}}^{\delta}$ and $\underline{\underline{\underline{\underline{\boldsymbol{I}}}}}^{+}$ have the following property:

$$\underline{\underline{\underline{\underline{\boldsymbol{I}}}}}^{\delta} : \underline{\underline{\boldsymbol{A}}} = \underline{\underline{\boldsymbol{A}}} : \underline{\underline{\underline{\underline{\boldsymbol{I}}}}}^{\delta} = \underline{\underline{\boldsymbol{I}}}\,\mathrm{trace}(\underline{\underline{\boldsymbol{A}}}), \tag{24}$$

$$\underline{\underline{\underline{\underline{\boldsymbol{I}}}}}^{+} : \underline{\underline{\boldsymbol{A}}} = \underline{\underline{\boldsymbol{A}}} : \underline{\underline{\underline{\underline{\boldsymbol{I}}}}}^{+} = \tfrac{1}{2}(\underline{\underline{\boldsymbol{A}}} + \underline{\underline{\boldsymbol{A}}}^{21}) \tag{25}$$

under double contraction : with any second-rank tensor $\underline{\underline{\boldsymbol{A}}}$; if $\underline{\underline{\boldsymbol{A}}} = A_{ij}\underline{\boldsymbol{e}}_i\underline{\boldsymbol{e}}_j$ (summation convention is understood) is given in components with regard to an orthonormal set $\underline{\boldsymbol{e}}_i$ ($i = 1, 2, 3$), then $\underline{\underline{\boldsymbol{A}}}^{21} = A_{ij}\underline{\boldsymbol{e}}_j\underline{\boldsymbol{e}}_i = A_{ji}\underline{\boldsymbol{e}}_i\underline{\boldsymbol{e}}_j$.

The infinite-space Green functions for the source field integrals read ($\underline{\boldsymbol{R}} \neq \underline{\boldsymbol{R}}'$) as

$$\underline{\underline{\boldsymbol{G}}}(\underline{\boldsymbol{R}} - \underline{\boldsymbol{R}}',\omega) = \frac{1}{\mu}\left[\left(\underline{\underline{\boldsymbol{I}}} + \frac{1}{k_{\mathrm{S}}^2}\nabla'\nabla'\right)G_{\mathrm{S}}(\underline{\boldsymbol{R}} - \underline{\boldsymbol{R}}',\omega) - \frac{1}{k_{\mathrm{S}}^2}\nabla'\nabla' G_{\mathrm{P}}(\underline{\boldsymbol{R}} - \underline{\boldsymbol{R}}',\omega)\right], \tag{26}$$

$$\underline{\underline{\underline{\underline{\boldsymbol{\Sigma}}}}}(\underline{\boldsymbol{R}} - \underline{\boldsymbol{R}}',\omega) = -\underline{\underline{\underline{\underline{\boldsymbol{c}}}}} : \nabla'\underline{\underline{\boldsymbol{G}}}(\underline{\boldsymbol{R}} - \underline{\boldsymbol{R}}',\omega), \tag{27}$$

$$\underline{\underline{\underline{\underline{\boldsymbol{\Pi}}}}}(\underline{\boldsymbol{R}} - \underline{\boldsymbol{R}}',\omega) = -[\nabla'\underline{\underline{\underline{\underline{\boldsymbol{\Sigma}}}}}(\underline{\boldsymbol{R}} - \underline{\boldsymbol{R}}',\omega)]^{2314} : \underline{\underline{\underline{\underline{\boldsymbol{c}}}}} \tag{28}$$

with P- and S-wavenumbers

$$k_{\mathrm{P}} = \omega\sqrt{\frac{\rho}{\lambda + 2\mu}}, \tag{29}$$

$$k_{\mathrm{S}} = \omega\sqrt{\frac{\rho}{\mu}} \tag{30}$$

and

$$G_{\mathrm{P,S}}(\underline{\boldsymbol{R}} - \underline{\boldsymbol{R}}',\omega) = \frac{\mathrm{e}^{\mathrm{j}k_{\mathrm{P,S}}|\underline{\boldsymbol{R}} - \underline{\boldsymbol{R}}'|}}{4\pi|\underline{\boldsymbol{R}} - \underline{\boldsymbol{R}}'|}. \tag{31}$$

Of course, $\underline{\underline{\underline{\underline{\boldsymbol{c}}}}}$ is always given by (23). As above, if $\underline{\underline{\underline{\underline{\boldsymbol{\Sigma}}}}} = \Sigma_{ijk}\underline{\boldsymbol{e}}_i\underline{\boldsymbol{e}}_j\underline{\boldsymbol{e}}_k$, then $\underline{\underline{\underline{\underline{\boldsymbol{\Sigma}}}}}^{321} = \Sigma_{ijk}\underline{\boldsymbol{e}}_k\underline{\boldsymbol{e}}_j\underline{\boldsymbol{e}}_i = \Sigma_{kji}\underline{\boldsymbol{e}}_i\underline{\boldsymbol{e}}_j\underline{\boldsymbol{e}}_k$; $[\nabla'\underline{\underline{\underline{\underline{\boldsymbol{\Sigma}}}}}]^{2314}$ follows from a similar definition.

Field-dependent equivalent sources

$$\underline{\boldsymbol{f}}_c(\underline{\boldsymbol{R}},\omega) = -\underline{\gamma}_c(\underline{\boldsymbol{R}}) \cdot \underline{\underline{\boldsymbol{T}}}(\underline{\boldsymbol{R}},\omega), \tag{32}$$

$$\underline{\underline{\boldsymbol{h}}}(\underline{\boldsymbol{R}},\omega) = -\underline{\underline{\underline{\boldsymbol{I}}}}^{+} : \underline{\gamma}_c(\underline{\boldsymbol{R}})\underline{\boldsymbol{v}}(\underline{\boldsymbol{R}},\omega) \tag{33}$$

yield the representation theorem

$$\underline{\boldsymbol{v}}_s(\underline{\boldsymbol{R}},\omega) = \iint_{S_c} [\mathrm{j}\omega\underline{\boldsymbol{n}}'_c \cdot \underline{\underline{\boldsymbol{T}}}(\underline{\boldsymbol{R}}',\omega) \cdot \underline{\underline{\boldsymbol{G}}}(\underline{\boldsymbol{R}}-\underline{\boldsymbol{R}}',\omega) - \underline{\boldsymbol{n}}'_c\underline{\boldsymbol{v}}(\underline{\boldsymbol{R}}',\omega) : \underline{\underline{\underline{\boldsymbol{\Sigma}}}}(\underline{\boldsymbol{R}}-\underline{\boldsymbol{R}}',\omega)]\,\mathrm{d}S' \tag{34}$$

due to the symmetry $\underline{\underline{\underline{\boldsymbol{\Sigma}}}} = \underline{\underline{\underline{\boldsymbol{\Sigma}}}}^{213}$, which results from a symmetry of $\underline{\underline{\underline{\boldsymbol{c}}}}$. In solids, the acoustical soft scatterer is characterized by a traction-free surface (a vacuum hole in a solid is a typical canonical defect in NDE). Hence, for such a class of scatterers we obtain

$$\underline{\boldsymbol{v}}_s(\underline{\boldsymbol{R}},\omega) = -\iint_{S_c} \underline{\boldsymbol{n}}'_c\underline{\boldsymbol{v}}(\underline{\boldsymbol{R}}',\omega) : \underline{\underline{\underline{\boldsymbol{\Sigma}}}}(\underline{\boldsymbol{R}}-\underline{\boldsymbol{R}}',\omega)\,\mathrm{d}S'. \tag{35}$$

Obviously, due to the superposition of P- and S-waves in (26), and consequently in (27), the inversion of (35), even after introducing the elastodynamic version of the linearizing Kirchhoff approximation, is even more complex than the inversion of (18). Fortunately, for far-field data we have

$$\underline{\underline{\underline{\boldsymbol{\Sigma}}}}^{\mathrm{far}}(\underline{\boldsymbol{R}},\underline{\boldsymbol{R}}',\omega) = \mathrm{j}k_\mathrm{P}\frac{\mathrm{e}^{\mathrm{j}k_\mathrm{P}R}}{4\pi R}(\lambda\underline{\underline{\boldsymbol{I}}} + 2\mu\hat{\underline{\boldsymbol{R}}}\hat{\underline{\boldsymbol{R}}})\hat{\underline{\boldsymbol{R}}} + \mathrm{j}k_\mathrm{S}\mu\frac{\mathrm{e}^{\mathrm{j}k_\mathrm{S}R}}{4\pi R}(\hat{\underline{\boldsymbol{R}}}\underline{\underline{\boldsymbol{I}}} + \hat{\underline{\boldsymbol{R}}}\underline{\underline{\boldsymbol{I}}}\hat{\underline{\boldsymbol{R}}}^{213} - 2\hat{\underline{\boldsymbol{R}}}\hat{\underline{\boldsymbol{R}}}\hat{\underline{\boldsymbol{R}}}) \tag{36}$$

exhibiting the fact that far-field scattered P-waves (first term of (36)) are strictly longitudinally polarized, whereas far-field scattered S-waves (second term of (36)) are strictly transversely polarized. Hence, mode separation is possible through polarization separation.

3. SAFT versus FT-SAFT

As already mentioned in the introduction, the Fourier transform is utilized as a convenient tool to switch between spaces, i.e. time and frequency domain. For instance, the Green function mathematics as discussed in the previous section is more lucid in the frequency domain. On the other hand, time domain interpretation in terms of wavefronts is physically more intuitive. This is the reason why *heuristic* approaches to wavefield inversion tend to prefer the time domain, this being particularly true for SAFT; the original reasoning and even the standard implementation by Müller and Schmitz (2002) is in the time domain. Nevertheless, if SAFT is embedded in a rigorous wavefield inversion theory (Langenberg 1987, 2002), the *a priori* choice of the frequency domain seems to be more appropriate to derive a general inversion formula, which, when obtained, can be transformed back to the time domain to yield—after several approximations—the SAFT scheme. In addition, this approach provides a frequency domain diffraction tomographic implementation alternative called FT-SAFT for Fourier-transform-SAFT.

3.1. SAFT: synthetic aperture focusing technique

Interestingly, there is no mathematical theory to derive SAFT, it is just simple reasoning with physically based arguments.

The simplest scatterer one can imagine is an acoustic point scatterer, its scattered field being proportional to the Green function (1), which reads in the time domain as

$$G(\underline{\boldsymbol{R}}-\underline{\boldsymbol{R}}',t) = \frac{\delta(t-\frac{|\underline{\boldsymbol{R}}-\underline{\boldsymbol{R}}'|}{c})}{4\pi|\underline{\boldsymbol{R}}-\underline{\boldsymbol{R}}'|}; \tag{37}$$

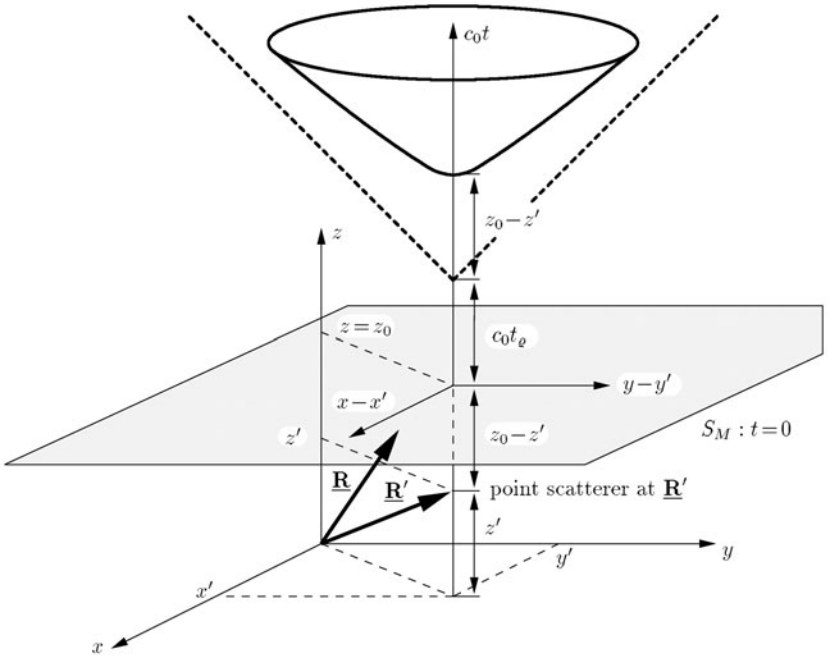

Figure 4. Diffraction surface of an acoustic point scatterer for a planar measurement surface S_M.

c is the acoustic wave speed $c = (\kappa\rho)^{-1/2}$. For a planar measurement surface, say the xy-plane of a Cartesian coordinate system, the diffraction surface in three-dimensional xyt-data space as defined by the support of the δ-distribution is a hyperboloid (figure 4). Hence, inversion (backpropagation) of this data space into object space requires (re)focusing the hyperboloid into the point scatterer located at $\underline{\boldsymbol{R}}'$. This is achieved by two different algorithmic versions of SAFT:

- A-scan-driven approach. Each xyt-data amplitude is equally distributed (backpropagated) on a spherical (isochronic) surface (Hagedoorn 1954, Bleistein and Gray 2001, Bleistein *et al* 2001); they all intersect at $\underline{\boldsymbol{R}}'$, where the scatterer resides.
- Pixel-driven approach. For each voxel (pixel in 2D) in discretized object space integration through data space along the pertinent hyperboloid is performed; the voxel containing $\underline{\boldsymbol{R}}'$ gets the highest amplitude.

In any case, an extended scatterer (defect) is considered to be an ensemble of point scatterers, which expresses the underlying linearizing approximation.

In practice, ultrasonic data are bandlimited; hence, the above SAFT versions will reproduce the time signal oscillations in image space. Our version of SAFT therefore applies backpropagation to the data as well as to the timely Hilbert-transformed data to create complex valued analytic signals in image space, where a subsequent magnitude calculation gets rid of the oscillations (Langenberg *et al* 1993a).

As far as P- and S-waves in solids are concerned, SAFT applies a time gating technique for mode separation and treats each wave as scalar.

The success of this imaging algorithm for ultrasonic NDE purposes is documented in the paper by Müller and Schmitz (2002), and the question of to what extent a solution of the inverse scattering problem is obtained has been answered by Langenberg (1987, 2002): SAFT

is basically a time domain (frequency diversity) backpropagation version of linear inverse scattering within the framework of diffraction tomography.

3.2. FT-SAFT

The close relationship of SAFT and diffraction tomography as outlined in detail by Langenberg (1987, 2002) suggests use of (scalar) far-field Fourier inversion as a speedy alternative (in particular in 3D), and to provide, if necessary, the far-field data through a near-field, far-field transform based on the representation theorem of Huygens' principle. As a matter of fact, this transform does not even need to be explicitly computed if the measurement surface is planar: in that case, and for far-field observation points, the representation integral (6) with $-\mathrm{j}\omega\rho\underline{\boldsymbol{n}}_c' \cdot \underline{\boldsymbol{v}} = -\nabla' p$ reduces to a two-dimensional Fourier integral

$$R\mathrm{e}^{-\mathrm{j}kR}\, p_s^{\mathrm{far}}(\underline{\boldsymbol{R}}, \omega) = -\frac{1}{4\pi}\left[\mathrm{j}k\underline{\hat{\boldsymbol{R}}} \cdot \underline{\boldsymbol{e}}_z \iint_{S_M} p_s(x', y', z', \omega)\mathrm{e}^{-\mathrm{j}k\underline{\hat{\boldsymbol{R}}}\cdot\underline{\boldsymbol{R}}'}\,\mathrm{d}x'\,\mathrm{d}y' + \iint_{S_M} \frac{\partial}{\partial z'} p_s(x', y', z', \omega)\mathrm{e}^{-\mathrm{j}k\underline{\hat{\boldsymbol{R}}}\cdot\underline{\boldsymbol{R}}'}\,\mathrm{d}x'\,\mathrm{d}y'\right]_{z'=z_0} \tag{38}$$

with regard to the measurement coordinates x', y' defining a Fourier vector $\underline{\boldsymbol{K}}'$ with components K_x', K_y', K_z' according to

$$\underline{\boldsymbol{K}}' = k\underline{\hat{\boldsymbol{R}}}, \tag{39}$$

$$K_z' = \sqrt{k^2 - K_x'^2 - K_y'^2}. \tag{40}$$

Through the mapping

$$\underline{\boldsymbol{K}} = \underline{\boldsymbol{K}}' - k\underline{\hat{\boldsymbol{k}}}_i, \tag{41}$$

i.e. (39) together with (11), the resulting Fourier-transformed data can be immediately organized in *far*-field $\underline{\boldsymbol{K}}$-space (Langenberg 2002).

The following example for a comparison of SAFT and FT-SAFT originates from NDE of concrete: here, a typical task is to locate metallic tendon ducts below the steel reinforcement, and electromagnetic ground probing radar systems have been found to contribute to the solution of this problem (Maierhofer *et al* 1995). Such systems provide (multi-)monostatic (pulse–echo) broadband (base band with approximately 1 GHz bandwidth) scalar data to be fed into (the *monostatic* versions of) SAFT and FT-SAFT, respectively (Mayer *et al* 1990). Aiming towards the experimental check of a bistatic (pitch–catch) *polarimetric* FT-SAFT algorithm (section 5), we performed a scalar monostatic free-space experiment in the 75–100 GHz range with an appropriately down-scaled model of a wire mesh above a steel rod (figure 5(*a*)): the images obtained from SAFT in figure 5(*b*) and FT-SAFT in figure 5(*c*)—here, the wire mesh plane has been selected—are nearly identical. But note that the one-slice-out-of-3D SAFT processing takes 40 min, whereas the complete 3D FT-SAFT processing (only one slice is displayed) takes 1.5 min on the same computer. With figure 6 we go into the depth of the 3D FT-SAFT imaging space to confirm that the tendon duct model—the rod—is monostatically visible below the wire mesh.

4. InASAFT: SAFT for inhomogeneous anisotropic materials

There is a rich variety of elastically anisotropic media, as specified by $\underline{\underline{\underline{\underline{\boldsymbol{c}}}}}$. In ultrasonic NDE, transversely isotropic media like fibre-reinforced composites or austenitic steel play an important role; they are described by five elastic constants $\lambda_\perp$, $\mu_\perp$, $\lambda_\parallel$, $\mu_\parallel$, ν and a preference

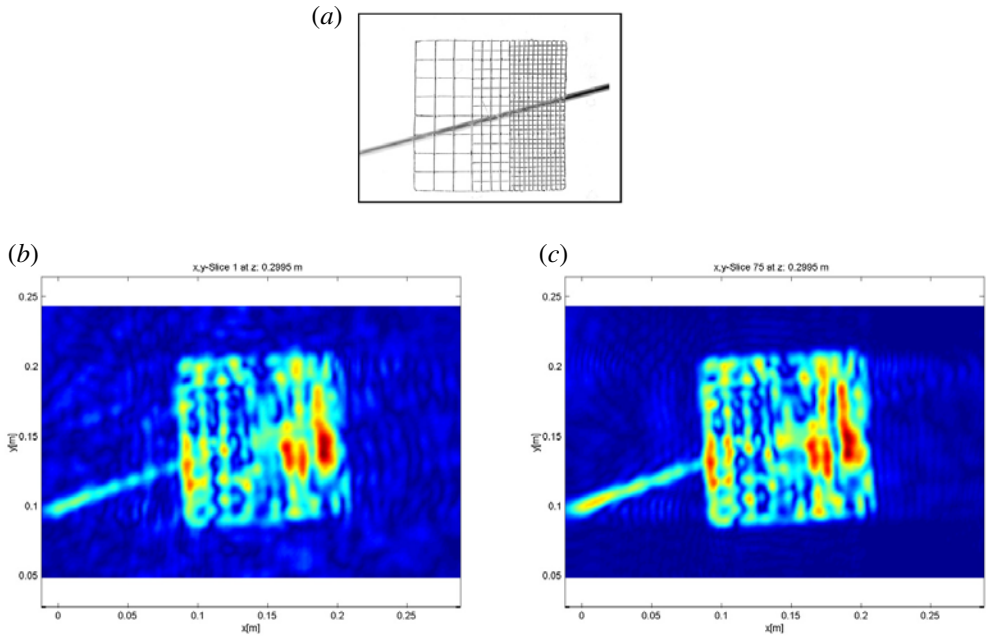

Figure 5. Comparison of SAFT and FT-SAFT.

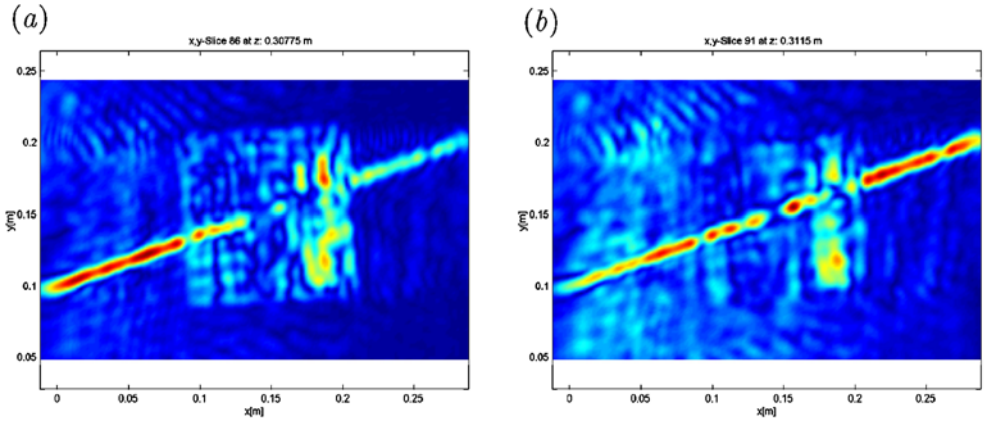

Figure 6. FT-SAFT imaging planes for the above model at two different depths below the wire mesh; the over-all size of the mesh is 112 × 112 mm^2, the spacing varying from 14 over 7 to 3.5 mm, the wire diameter is 0.8 mm, the rod diameter 10 mm.

direction $\underline{\hat{a}}$ (the fibre direction, the crystal orientation); orthogonal to $\underline{\hat{a}}$, the material is isotropic. For these materials $\underline{\underline{\underline{c}}}$ reads (Spies 1992, Marklein 1997)

$$\underline{\underline{\underline{c}}} = \lambda_\perp \underline{\underline{\underline{I}}}^{\delta} + 2\mu_\perp \underline{\underline{\underline{I}}}^{+} + \alpha_1 \underline{\hat{a}}\,\underline{\hat{a}}\,\underline{\hat{a}}\,\underline{\hat{a}} + \alpha_2(\underline{\underline{I}}\,\underline{\hat{a}}\,\underline{\hat{a}} + \underline{\hat{a}}\,\underline{\hat{a}}\,\underline{\underline{I}}) + \alpha_3(\underline{\underline{I}}\,\underline{\hat{a}}\,\underline{\hat{a}} + \underline{\hat{a}}\,\underline{\hat{a}}\,\underline{\underline{I}})^{1324} + \alpha_3(\underline{\underline{I}}\,\underline{\hat{a}}\,\underline{\hat{a}} + \underline{\hat{a}}\,\underline{\hat{a}}\,\underline{\underline{I}})^{1342} \tag{42}$$

with

$$\alpha_1 = \lambda_\perp + 2\mu_\perp + \lambda_\parallel + 2\mu_\parallel - 2(\nu + 2\mu_\parallel), \tag{43}$$

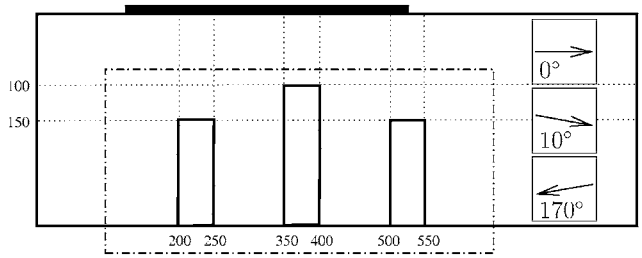

Figure 7. Test geometry for ASAFT.

$$\alpha_2 = \nu - \lambda_\perp, \tag{44}$$

$$\alpha_3 = \mu_\parallel - \mu_\perp. \tag{45}$$

In contrast to the degeneracy of isotropic materials, plane qP- and qS-wave[2] phase- and energy velocities depend on the propagation direction $\hat{\underline{\underline{k}}}$, and the direction of the energy velocity is always perpendicular to the slowness surface. Since ultrasonic signal recording is with regard to the energy propagation direction, algorithmic data processing must properly account for it in order to locate and size defects exactly. As we pointed out in section 2, the availability of Green functions is mandatory, but, unfortunately, explicit expressions similar to (26)–(28) are not available for transversely isotropic media. But it turns out that the geometrical shapes of time domain wavefronts emanating from point sources are identical to the so-called wave surfaces of plane wave energy diagrams (Helbig 1994, Snieder 2002, Langenberg *et al* 2002); hence, with (37) the Green function expression (26) could be generalized to

$$\underline{\underline{G}}^{\text{triso}}(\underline{\underline{R}} - \underline{\underline{R}}', t) = \underline{\underline{G}}_{\text{qS}}(\underline{\underline{R}} - \underline{\underline{R}}', t) * \frac{\delta\left(t - \frac{|\underline{\underline{R}} - \underline{\underline{R}}'|}{c_{\text{EqS}}(\hat{\underline{\underline{l}}})}\right)}{|\underline{\underline{R}} - \underline{\underline{R}}'|} + \underline{\underline{G}}_{\text{qP}}(\underline{\underline{R}} - \underline{\underline{R}}', t) * \frac{\delta\left(t - \frac{|\underline{\underline{R}} - \underline{\underline{R}}'|}{c_{\text{EqP}}(\hat{\underline{\underline{l}}})}\right)}{|\underline{\underline{R}} - \underline{\underline{R}}'|}, \tag{46}$$

where $c_{\text{EqP,qS}}(\hat{\underline{\underline{l}}})$ are qP- and qS-wave energy velocities as a function of the ray vector $\hat{\underline{\underline{l}}} = (\underline{\underline{R}} - \underline{\underline{R}}')/|\underline{\underline{R}} - \underline{\underline{R}}'|$; the asterisk stands for a t-convolution integral. Now, as stated before, the tensor amplitudes $\underline{\underline{\underline{G}}}_{\text{qP,qS}}$ are not known, and, hence, within a first approximation a SAFT algorithm for homogeneous anisotropic materials could be based on the δ-functions in (46) only: this is ASAFT.

We turn to an example given by Hannemann (2002) with synthetic (bistatic, pitch–catch) data as produced with the numerical EFIT code (elastodynamic finite integration technique: Fellinger *et al* 1995, Marklein 1997). Figure 7 shows the (two-dimensional) geometry (scales in mm): an austenitic steel block (austenitic steel 308) contains three notches with different heights, and the preference direction $\hat{\underline{\underline{a}}}$ of the homogeneous material has been chosen subsequently according to the three arrows; the fat bar on top indicates the 400 mm wide measurement aperture, excitation is a 45° P-wave transducer with an aperture width of 12 mm centred with respect to the measurement aperture.

Figure 8 compares qP-slowness and -energy velocity diagrams of this kind of transversely isotropic austenitic steel and isotropic ferritic steel; obviously, the differences for the qP-wave mode are not very large. Nevertheless, the SAFT imaging results (figures 9(*a*), (*c*), (*e*)) exhibit strongly misplaced corners of the notches whereas ASAFT locates them correctly (figures 9(*b*), (*d*), (*f*)).

[2] In anisotropic materials primary waves are only quasi-pressure (qP-)waves and secondary waves are only quasi-shear (qS-)waves; qS-waves appear in two orthogonal polarizations.

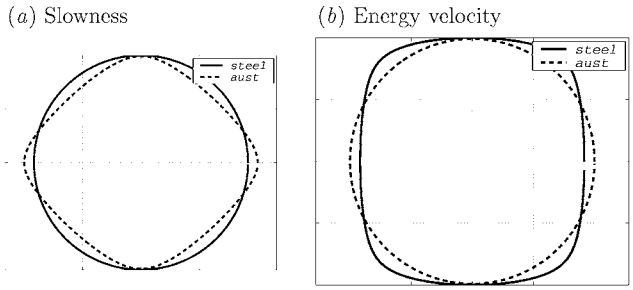

Figure 8. qP-slowness and energy velocity diagrams for ferritic and austenitic steel; $\hat{\underline{a}}$ is horizontally oriented.

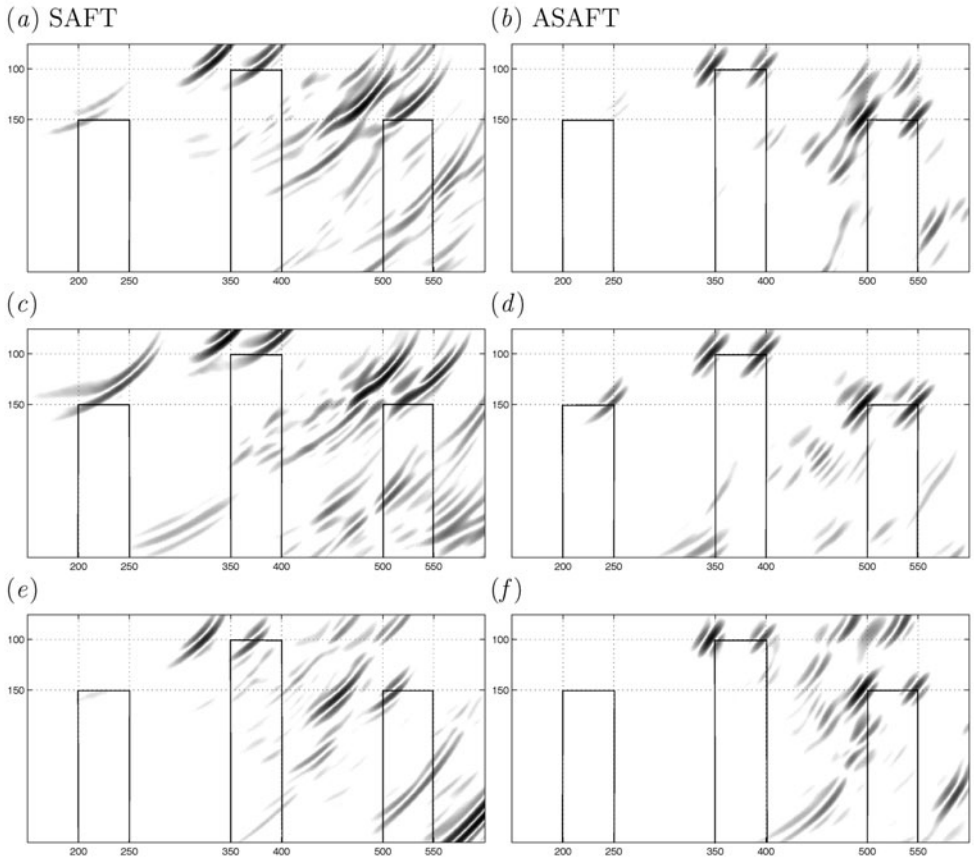

Figure 9. SAFT (left) and ASAFT (right) imaging results for three different $\hat{\underline{a}}$-orientations: 0°, 10° and 170° from top to bottom.

Based on the same imaging principle, ASAFT has been extended to pixelwise inhomogeneous anisotropic materials (InASAFT: Hannemann 2002); for each A-scan one starts with equally spaced slowness directions in the first pixel and computes the corresponding energy ray directions as being orthogonal to the slowness surface; at the first interface, for a particular selected energy ray, phase matching for the corresponding slowness produces the slowness direction in the adjacent pixel, which is then again transformed into the

corresponding energy direction; reflected and mode-converted rays are disregarded, and transmission coefficients are set equal to one. Having obtained all ray paths, travel times are computed on the basis of the pertinent energy velocities according to the Green function approximation. This algorithm is presently under check for experimental data obtained within a joint European project (Dikstra and Cameron 2002).

5. Electromagnetic vector diffraction tomography

Electromagnetic and ultrasonic imaging in solids should account for the proper polarization of any wave mode. For electromagnetic waves this means that (20) together with (21) should be under concern for inversion. Choosing

$$\underline{\boldsymbol{E}}_i(\underline{\boldsymbol{R}}, \omega) = E_0(\omega)\, \mathrm{e}^{\mathrm{j}k\underline{\hat{\boldsymbol{k}}}_i \cdot \underline{\boldsymbol{R}}}\, \underline{\hat{\boldsymbol{E}}}_0 \tag{47}$$

as the linearly polarized incident field with frequency spectrum $E_0(\omega)$ we obtain ($Z = \sqrt{\mu_0\mu_r/\epsilon_0\epsilon_r}$)

$$\underline{\boldsymbol{H}}_i(\underline{\boldsymbol{R}}, \omega) = \frac{E_0(\omega)}{Z}\, \underline{\hat{\boldsymbol{k}}}_i \times \underline{\hat{\boldsymbol{E}}}_0\, \mathrm{e}^{\mathrm{j}k\underline{\hat{\boldsymbol{k}}}_i \cdot \underline{\boldsymbol{R}}} \tag{48}$$

and

$$\underline{\boldsymbol{J}}_{\mathrm{ec}}^{\mathrm{PO}}(\underline{\boldsymbol{R}}, \omega) = E_0(\omega) \underbrace{\frac{2}{Z}\, \underline{\gamma}_u(\underline{\boldsymbol{R}}) \times (\underline{\hat{\boldsymbol{k}}}_i \times \underline{\hat{\boldsymbol{E}}}_0)}_{= \underline{\boldsymbol{J}}_c(\underline{\boldsymbol{R}})}\, \mathrm{e}^{\mathrm{j}k\underline{\hat{\boldsymbol{k}}}_i \cdot \underline{\boldsymbol{R}}}. \tag{49}$$

For any smooth surface S_c with singular function $\underline{\gamma}_c(\underline{\boldsymbol{R}})$ we have

$$\nabla \times \underline{\gamma}_c(\underline{\boldsymbol{R}}) = \underline{\mathbf{0}}, \tag{50}$$

and, hence,

$$\nabla \times \underline{\gamma}_u(\underline{\boldsymbol{R}}) = \delta(-\underline{\hat{\boldsymbol{k}}}_i \cdot \underline{\boldsymbol{n}}_c)\underline{\gamma}_c(\underline{\boldsymbol{R}}) \times \nabla(\underline{\hat{\boldsymbol{k}}}_i \cdot \underline{\boldsymbol{n}}_c) = \underline{\mathbf{0}} \tag{51}$$

is postulated, since a shadow *line* on S_c is only somewhat arbitrarily introduced by $\delta(-\underline{\hat{\boldsymbol{k}}}_i \cdot \underline{\boldsymbol{n}}_c)$ resulting from the PO approximation. From (51) and (49) we deduce

$$\nabla \cdot \underline{\boldsymbol{J}}_c(\underline{\boldsymbol{R}}) = 0, \tag{52}$$

which yields (the tilde characterizes the three-dimensional Fourier transform with respect to $\underline{\boldsymbol{R}}$)

$$\underline{\boldsymbol{K}} \cdot \tilde{\underline{\boldsymbol{J}}}_c(\underline{\boldsymbol{K}}) = 0; \tag{53}$$

this, together with (11), reduces the operator $\underline{\underline{\boldsymbol{I}}} - \underline{\hat{\boldsymbol{R}}}\,\underline{\hat{\boldsymbol{R}}}$ to $\underline{\underline{\boldsymbol{I}}} - (\underline{\boldsymbol{K}} + k\underline{\hat{\boldsymbol{k}}}_i)\underline{\hat{\boldsymbol{k}}}_i / k$, which is invertible. Therefore, the vector function $\underline{\boldsymbol{J}}_c(\underline{\boldsymbol{R}})$ can be deduced from a far-field Fourier inversion scheme, and, as in the scalar case, a near-field, far-field transform can be avoided applying the vector representation theorem of the electromagnetic Huygens principle together with the mapping rule (41) (Brandfaß 1996).

Various applications of this electromagnetic vector diffraction tomographic algorithm to synthetic data gave superior results to pure scalar inversion operating on the scalar components of the scattered electric field strength (Langenberg *et al* 1994, 1999a, 1999b, Brandfaß 1996). The most convincing results were obtained for synthetic scattering data for an air plane model obtained with the MAFIA code (Bartsch *et al* 1990, Brandfaß 1996, Langenberg *et al* 1999a). Hence, we performed a bistatic polarimetric experiment for an appropriately down-scaled model in the 75–100 GHz range (the same experimental setup as was utilized to obtain the results of figures 5 and 6). Even though this is not yet an NDE-related experiment, it should at

least prove the practicability of experimental polarimetric inversion. Figure 10 shows results: the air plane model is illuminated orthogonally to the wings with a horn antenna in a distance of 300 mm, and a second identical horn antenna scans the bistatic electric field strength components along a plane in the backscattering direction for the same distance; horizontal polarization denotes the component of the electric field strength orthogonal to the fuselage, and vertical polarization denotes the respective component parallel to the fuselage. Obviously, the superimposed polarimetric image is more complete than the single scalar images, which contain complementary information. This generally confirms the numerical experiments with synthetic data (Brandfaß 1996, Langenberg *et al* 1999a). Note that all 2D images in figure 10 are obtained by adding up the single image planes of three-dimensional image space.

Returning to NDE, the air plane model is replaced by the mesh–rod model of figure 5, and the same bistatic electromagnetic experiment as before is performed. The actual available results are given in figure 11.

First, cross-polarized data are way down in amplitude as compared to the co-polarization data, and both co-polarizations yield approximately similar images. Hence, an algorithmic superposition does not seem appropriate. Second, the bistatic scalar result, even though given for two different polarizations, is less convincing than the monostatic result of figures 5 and 6. This is particularly disappointing at the moment, because the numerical experiments on synthetic data performed much better (Brandfaß 1996, Langenberg *et al* 1999b). The reason might be a violation of some algorithmic assumption, e.g. the replacement of plane wave by strongly directive horn antenna illumination, which is particularly serious for this kind of geometry in contrast to our air plane model.

For ultrasonic applications, vector diffraction tomography is additionally concerned with the superposition of primary and secondary wave modes. As a matter of fact, an elastodynamic version of FT-SAFT, called EL-FT-SAFT, has been realized via a mode-selective (through far-field polarization) far-field Fourier inversion together with a $\underline{\boldsymbol{K}}$-space mapped near-field, far-field transform (Kostka 2000, Kostka *et al* 1998). Here, experimental results could confirm the practicability (Langenberg *et al* 1999b, 2002).

6. Nonlinear inversion

The nonlinear nature of the inverse scattering problem has been disregarded in the previous sections. All versions of SAFT and FT-SAFT together with their polarimetric extensions are linear algorithms. In this section we present some inversion results applying nonlinear inverse scattering schemes, where we focus on the *scalar* case. For applications in ultrasonic NDE, this means that we consider a specific wave mode as scalar, here the P-wave. In fact, various approaches have been formulated, which try to solve the nonlinear scalar inverse scattering problem with more or less approximations:

- extended Born method (see e.g. Habashy *et al* 1993)
- iterative Born method (see e.g. Tijhuis 1989)
- distorted Born or Newton–Kantorovich method (see e.g. Roger 1981, Chew and Wang 1990, Franchois 1993)
- modified gradient method (MGF) (see e.g. Kleinman and van den Berg 1992, 1994, Pelekanos 1997, Haak 1999, Pelekanos *et al* 2000)
- contrast source inversion (CSI) (see e.g. Kleinman and van den Berg 1997, Haak 1999, van den Berg *et al* 1999)
- extended contrast source inversion (ECSI) (see e.g. van den Berg *et al* 1999, Abubakar 2000)

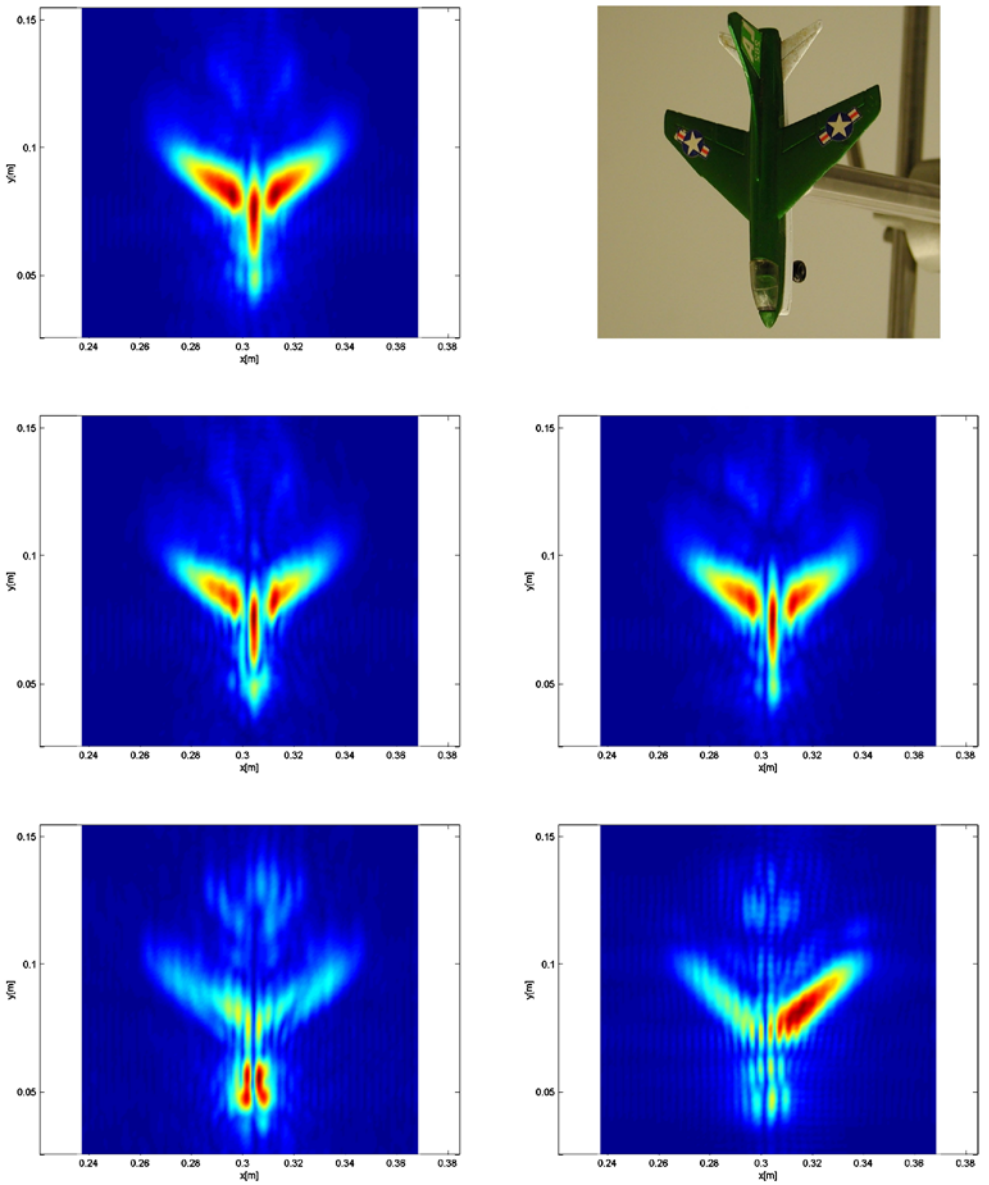

Figure 10. Bistatic polarimetric image (top left) of an air plane model (top right) obtained by scalar algorithmic superposition of horizontal–horizontal co-, vertical–vertical co-, horizontal–vertical cross- and vertical–horizontal cross-polarization (middle left, middle right, bottom left, bottom right respectively); the model is 103 mm long with a wingspan of 85 mm.

- linear sampling method (LSM) (see e.g. Colton and Kirsch 1996, Colton *et al* 1997, Kirsch 1998, 1999, Arens 2001)
- approximate inverse method (AIM) (see e.g. Louis 1995, 1996, Abdullah and Louis 1999)
- real-coded genetic algorithm (RGA) (see e.g. Qing 2001, Qing *et al* 2001)
- and others.

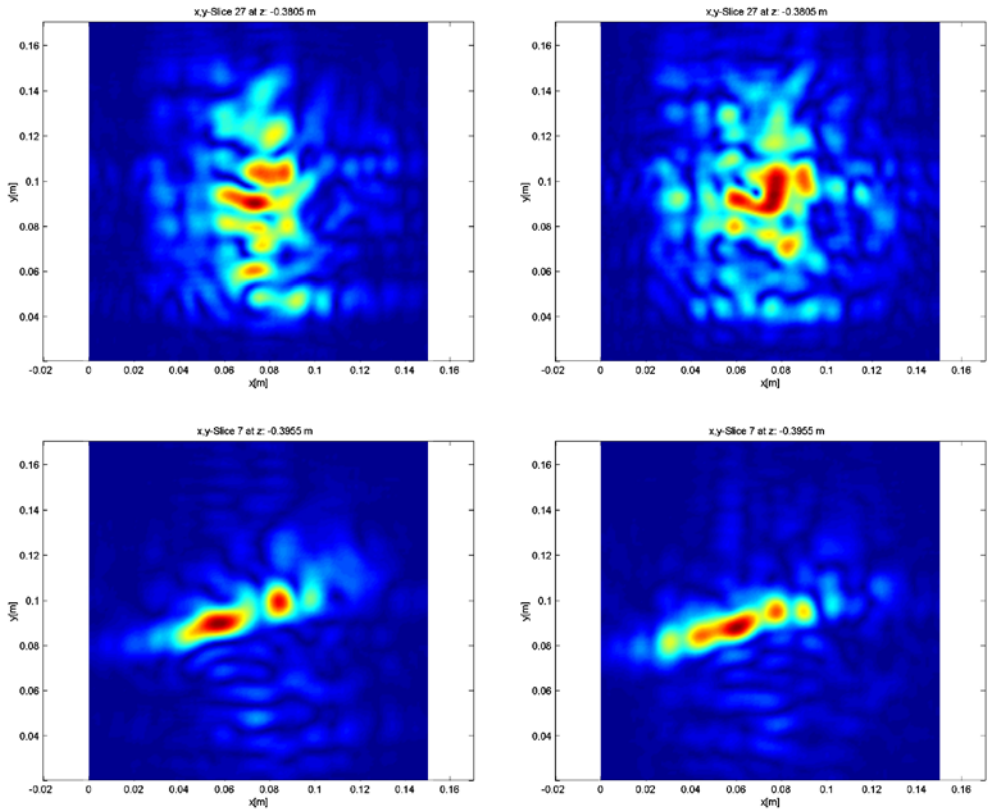

Figure 11. Scalar horizontal–horizontal (left) and vertical–vertical (right) co-polarization images of a mesh–rod model in two different depths (top: plane of the mesh; bottom: plane of the rod).

A comparative study of the performance of the majority of the above algorithms has been reported by van den Berg (1999, 2001), Marklein *et al* (2001).

The applications of most of the above-mentioned methods in electromagnetic or ultrasonic NDE are still very few. Here, we will apply two versions of the CSI method for the scalar nonlinear inverse scattering problem:

- the CSI method with weighted contrast sources (CSIW) and
- the ECSI method.

Both have been successfully validated using real electromagnetic inverse scattering data for remote sensing and geophysical prospecting, see e.g. the special sections in *IEEE Transactions on Antennas and Propagation Magazine* (McGahan and Kleinman 1996, 1997, 1999a, 1999b) and the special section in *Inverse Problems* (2001) on 'Testing inversion algorithms against experimental data'.

In the CSIW and ECSI method the inverse problem is posed as an optimization problem, where a cost functional given in terms of the domain integral equations is iteratively minimized. An important advantage of these methods is to avoid the full solution of the underlying direct problem in each iteration by updating two unknowns simultaneously.

A sketch of the scattering problem is given in figure 12. We consider an inhomogeneous scatterer V_c immersed in a homogeneous background V_D. The ith transmitting and receiving

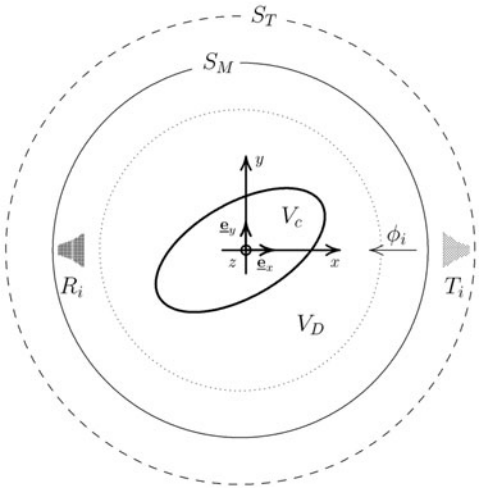

Figure 12. Experimental setup for the direct and inverse scattering problem.

ultrasonic transducers, T_i and R_i, are placed at the transmitter and measurement surface, S_T and S_M, enclosing the scattering domain V_c. The total field inside the domain V_D is given by the superposition of the (scalar) incident and scattered field:

$$\phi(\underline{\boldsymbol{R}}, \omega) = \phi_i(\underline{\boldsymbol{R}}, \omega) + \phi_s(\underline{\boldsymbol{R}}, \omega).$$

It has been shown (see, for example, Colton and Kress 1998) that the field ϕ satisfies the following domain integral equation (*Lippman–Schwinger equation*; object equation) for $\underline{\boldsymbol{R}} \in V_D$:

$$\phi(\underline{\boldsymbol{R}}, \omega) = \phi_i(\underline{\boldsymbol{R}}, \omega) + k^2 \iiint_{V_D} G(\underline{\boldsymbol{R}} - \underline{\boldsymbol{R}}', \omega)\chi(\underline{\boldsymbol{R}}', \omega)\phi(\underline{\boldsymbol{R}}', \omega)\,\mathrm{d}^3\underline{\boldsymbol{R}}'. \tag{54}$$

For $\underline{\boldsymbol{R}} \in S_M$ we have

$$\phi_s(\underline{\boldsymbol{R}}, \omega) = k^2 \iiint_{V_D} G(\underline{\boldsymbol{R}} - \underline{\boldsymbol{R}}', \omega)\,\chi(\underline{\boldsymbol{R}}', \omega)\,\phi(\underline{\boldsymbol{R}}', \omega)\,\mathrm{d}^3\underline{\boldsymbol{R}}', \tag{55}$$

which is the so-called *data equation*; $G(\underline{\boldsymbol{R}} - \underline{\boldsymbol{R}}', \omega)$ according to (1) denotes the Green function of the homogeneous background and $\chi(\underline{\boldsymbol{R}})$ is the contrast function defined as

$$\chi(\underline{\boldsymbol{R}}) = \begin{cases} \dfrac{k^2(\underline{\boldsymbol{R}})}{k^2} - 1, & \underline{\boldsymbol{R}} \in V_c \\ 0, & \underline{\boldsymbol{R}} \in \mathbb{R}^3 \backslash V_c, \end{cases} \tag{56}$$

where k is the wavenumber of the homogeneous background and $k(\underline{\boldsymbol{R}})$ represents the wavenumber function of the (unknown) inhomogeneous scatterer.

In the above two equations the incident field $\phi_i(\underline{\boldsymbol{R}}, \omega)$ is usually assumed as a plane wave and the scattered field $\phi_s(\underline{\boldsymbol{R}}, \omega)$ is supposed to be known from measurements. The unknown to be determined is the contrast function $\chi(\underline{\boldsymbol{R}})$.

Introducing the operators for $\underline{\boldsymbol{R}} \in V_D, S_M$

$$\mathcal{G}_{V_D, S_M}\{\bullet\} = k^2 \iiint_{V_D} G(\underline{\boldsymbol{R}} - \underline{\boldsymbol{R}}', \omega)\,\{\bullet\}\,\mathrm{d}^3\underline{\boldsymbol{R}}' \tag{57}$$

turns (54) and (55) into

$$\phi_i(\underline{\boldsymbol{R}},\omega) = \phi(\underline{\boldsymbol{R}},\omega) - \mathcal{G}_{V_D}\{\chi(\,\cdot\,,\omega)\,\phi(\,\cdot\,,\omega)\}(\underline{\boldsymbol{R}}), \tag{58}$$

$$\phi_s(\underline{\boldsymbol{R}},\omega) = \mathcal{G}_{S_M}\{\chi(\,\cdot\,,\omega)\phi(\,\cdot\,,\omega)\}(\underline{\boldsymbol{R}}). \tag{59}$$

The product of the contrast and the total field

$$w(\underline{\boldsymbol{R}},\omega) = \chi(\underline{\boldsymbol{R}},\omega)\,\phi(\underline{\boldsymbol{R}},\omega) \tag{60}$$

is called the contrast source, which can be considered as an equivalent source generating the measured scattered field, since the total field ϕ satisfies the equation

$$(\Delta + k^2)\phi(\underline{\boldsymbol{R}},\omega) = -k^2\, w(\underline{\boldsymbol{R}},\omega). \tag{61}$$

With (58) and (59) we deduce

$$\chi(\underline{\boldsymbol{R}},\omega)\phi_i(\underline{\boldsymbol{R}},\omega) = w(\underline{\boldsymbol{R}},\omega) - \chi(\underline{\boldsymbol{R}},\omega)G_{V_D}\{w(\,\cdot\,,\omega)\}(\underline{\boldsymbol{R}}), \tag{62}$$

$$\phi_s(\underline{\boldsymbol{R}},\omega) = G_{S_M}\{w(\,\cdot\,,\omega)\}(\underline{\boldsymbol{R}}). \tag{63}$$

A rough outline of the nonlinear CSIW and ECSI inversion schemes reads as follows.

- The weighted contrast source inversion (CSIW) method is a variation of the CSI method using instead of the contrast source and field their weighted counterparts

$$\tilde{w}(\underline{\boldsymbol{R}},\omega) = \frac{w(\underline{\boldsymbol{R}},\omega)}{\phi_i(\underline{\boldsymbol{R}},\omega)} \qquad \text{and} \qquad \tilde{\phi}(\underline{\boldsymbol{R}},\omega) = \frac{\phi(\underline{\boldsymbol{R}},\omega)}{\phi_i(\underline{\boldsymbol{R}},\omega)} \tag{64}$$

(see Kleinman and van den Berg 1997, Haak 1999). This results in weighted object and data equations

$$\chi(\underline{\boldsymbol{R}},\omega) = \tilde{w}(\underline{\boldsymbol{R}},\omega) - \frac{\chi(\underline{\boldsymbol{R}},\omega)}{\phi_i(\underline{\boldsymbol{R}},\omega)}G_{V_D}\{\phi_i(\cdot,\omega)\tilde{w}(\cdot,\omega)\}(\underline{\boldsymbol{R}}), \tag{65}$$

$$\phi_s(\underline{\boldsymbol{R}},\omega) = G_{S_M}\{\phi_i(\,\cdot\,,\omega)\,\tilde{w}(\,\cdot\,,\omega)\}(\underline{\boldsymbol{R}}). \tag{66}$$

The nonlinear inverse scattering scheme consists of three steps:

(i) Calculation of the weighted contrast source $\tilde{w}(\underline{\boldsymbol{R}},\omega)$ by minimizing the misfit in the object and data equations—(65) and (66)—using a conjugate gradient update. In the first iteration an initial value for the contrast is assumed and in the subsequent iterations the contrast in the previous iteration is used instead of $\chi(\underline{\boldsymbol{R}},\omega)$.

(ii) Computation of the weighted total field $\tilde{\phi}(\underline{\boldsymbol{R}},\omega)$ using the weighted equivalent of (62)

$$\tilde{\phi}(\underline{\boldsymbol{R}},\omega) = 1 + \frac{1}{\phi_i(\underline{\boldsymbol{R}},\omega)}G_{V_D}\{\phi_i(\,\cdot\,,\omega)\tilde{w}(\,\cdot\,,\omega)\}(\underline{\boldsymbol{R}}). \tag{67}$$

(iii) Reconstruction of the contrast function minimizing the misfit in the definition of the weighted contrast source:

$$\tilde{w}(\underline{\boldsymbol{R}},\omega) = \chi(\underline{\boldsymbol{R}},\omega)\tilde{\phi}(\underline{\boldsymbol{R}},\omega). \tag{68}$$

This equation is minimized for

$$\chi(\underline{\boldsymbol{R}},\omega) = \frac{\tilde{w}(\underline{\boldsymbol{R}},\omega)\tilde{\phi}^*(\underline{\boldsymbol{R}},\omega)}{|\tilde{\phi}(\underline{\boldsymbol{R}},\omega)|^2}. \tag{69}$$

In the above equation the star '*' denotes conjugate complex.

The CSIW can work for both penetrable and perfect scatterers as well as with or without *a priori* information. Regularization methods using total variation (TV) can be used for stabilizing the convergence of the CSIW method (see e.g. Abubakar and van den Berg (2001) and references therein), but this has not been implemented for our applications.

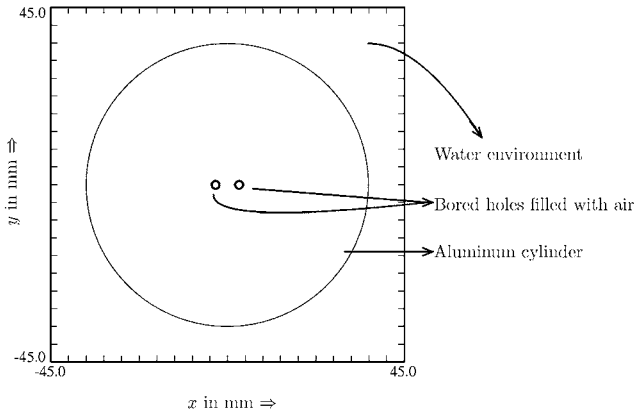

Figure 13. Experimental setup for the ultrasonic IZFP data set.

Table 1. Parameters of ultrasonic IZFP data set

Background	Aluminium cylinder with a radius of 36 mm
Scatterer	Two air-filled cylindrical holes with a diameter of 2 mm and separated by a distance of 4 mm
Wave type	Ultrasonic waves (P wave processed only)
Wave speed of P wave	$c_{\mathrm{P}} = 6297$ m s^{-1}
Transient pulse excitation	Transient signal with a bandwidth from 3.75 to 7 MHz
Multi-pulse–echo	Transceivers: 360 at a radius of 70 mm, each 1° apart
Multi-pitch–catch	Transmitters: 360 at a radius of 70 mm, each 1° apart Receivers: 340 at a radius of 55 mm, each 1° apart

- The ECSI method is an extended version of the CSI method (van den Berg *et al* 1999). In the CSI method, the contrast for each iteration is computed analytically using (69), but the total misfit in the object and data equations may not decrease using this formula. To overcome this difficulty, the ECSI method is introduced where the reduction in the total misfit is guaranteed by updating the contrast using a line minimization algorithm. This helps to introduce an extra minimization term for the residual function representing the TV of the contrast. To avoid a tuning process which is needed if an additive TV term is used, van den Berg *et al* (1999) introduced a multiplicative TV term. This has been implemented for our applications, yet it has been completely unsuccessful in inverting the experimental data given in the following section; the multiplicative TV regularization worked only for synthetic data. Obviously, research has to continue in this direction to obtain successful results on experimental data using regularization.

6.1. Inversion example related to ultrasonic NDE

As a canonical (two-dimensional) inversion example related to ultrasonic NDE we present results of the reconstruction of two air-filled cylindrical holes in an aluminium cylinder immersed in a water tank as obtained with SAFT, CSIW and ECSI. An outline of the experiment is shown in figure 13. Two ultrasonic transducers are positioned on a circle around the aluminium cylinder focusing on its surface. Two data sets have been measured representing two typical NDE measurement techniques:

- a multi-pulse–echo (multi-monostatic) data set and
- a multi-pitch–catch (multi-bistatic) data set.

For the multi-pulse–echo data set an ultrasonic transducer operating in pulse–echo mode on a measurement circle around the aluminium cylinder records A-scans for 360 positions each 1° apart. For the multi-pitch–catch data set 340 receiver positions are chosen for any one of the 360 emitter positions each 1° apart. The most important parameters of the experiment are summarized in table 1.

The multi-pulse–echo data set is processed with the time domain SAFT algorithm, and the multi-pitch–catch data set is processed with the linear time domain SAFT and the nonlinear frequency domain CSIW and ECSI algorithms.

6.1.1. Processing and inversion of the multi-pulse–echo (multi-monostatic) data set. The transceiver output is a bandlimited time domain signal between 3.75 and 7 MHz which is digitized at 80 MHz and stored in a computer. The complete multi-pulse–echo data set is plotted in figure 14. The transducer is placed on a measurement circle S_M with a radius of 70 mm and transmits a transient bandlimited pulse. The transmitted transient incident wave is first reflected by the near-boundary of the aluminium cylinder, which is to be recorded first, followed by the echoes from the two holes. Finally, the return echo from the far-boundary of the aluminium cylinder is recorded. The time between the near-boundary echo and the far-boundary echo corresponds to a distance equal to twice the diameter of the cylinder. Figure 14 shows 2580 time samples for each of the 360 transceiver positions placed around the cylinder. In this pulse–echo case the scattered field from the two holes can be time gated and given as input in the SAFT algorithm. The exact geometry of the scatterers is shown in figure 15(a). The imaging result using the time domain SAFT is shown in figure 15(b). The CSIW and the ECSI algorithms could not yield noteworthy results with this multi-pulse–echo data set and, hence, they are not shown here. The domain V_D is confined to 10×10 mm^2 within the aluminium cylinder being discretized by a grid of 256×256 pixels. Here, all 360 transceiver positions have been used to obtain the displayed image. Obviously, the boundaries of the holes are clearly visible but the image is not free of ghost artifacts.

6.1.2. Processing and inversion of the multi-pitch–catch (multi-bistatic) data set. In this case, the total time domain field is measured at 340 receiver positions for any of the 360 transmitter positions around the cylinder. All positions are separated by an angle of 1°. Using many receiver positions for one transmitter position provides angular diversity for each transmitter position, which is absent in the multi-pulse–echo data set. Figure 16 shows the data set plot obtained for 340 receivers and a transmitter placed at an angle of 0°. Again, the sampling frequency is 80 MHz and the total time corresponds to 16.75 μs. Similar data sets are recorded for the other 359 transmitter positions. In contrast to the previous data set, these data sets contain the incident field as well, yet the algorithms, especially CSIW and ECSI, only operate on the scattered field, hence the incident field must be removed. After several trials, the following method was adopted: the total field data—similar to those shown in figure 16—are added up for all transmitters, which generate predominantly incident field data, as the scattered echo is different for different transmitters. The incident field obtained that way is subtracted from each data set to yield the scattered field data.

The time domain data set obtained by the above procedure is ready to be used as input to the time domain SAFT algorithm, but the CSIW and ECSI algorithms need frequency domain data. Hence, the time domain signals are Fourier transformed into the frequency domain using an FFT routine, and the complex amplitudes are selected at some single discrete frequencies.

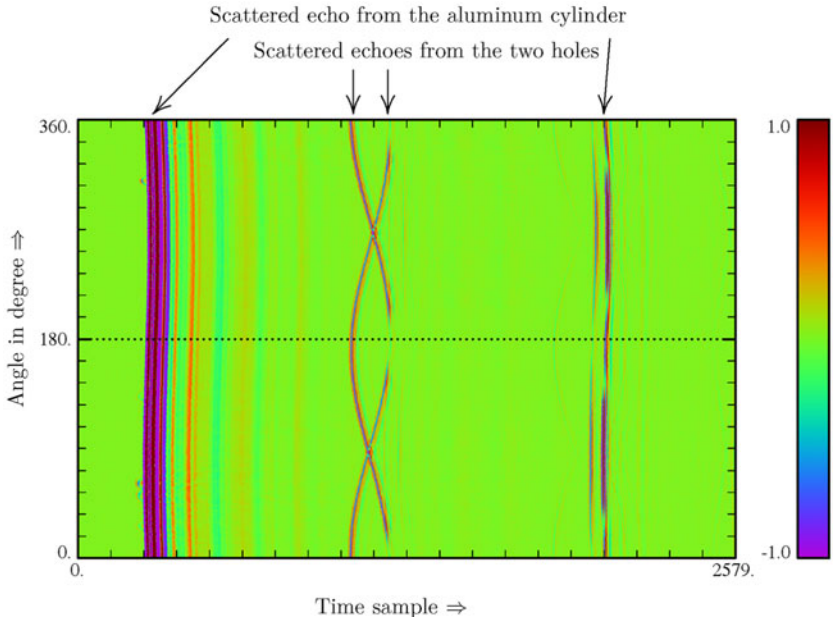

Figure 14. Measured ultrasonic pulse–echo (multi-monostatic) time domain data set. The voltage output of the transducer is plotted, which is normalized by the maximum value. The vertical axis shows the position angle of the transducer in degrees. The horizontal axis shows the time samples for a total time of 32.25 μs. The sampling frequency is 80 MHz corresponding to a sampling distance of 12.5 ns.

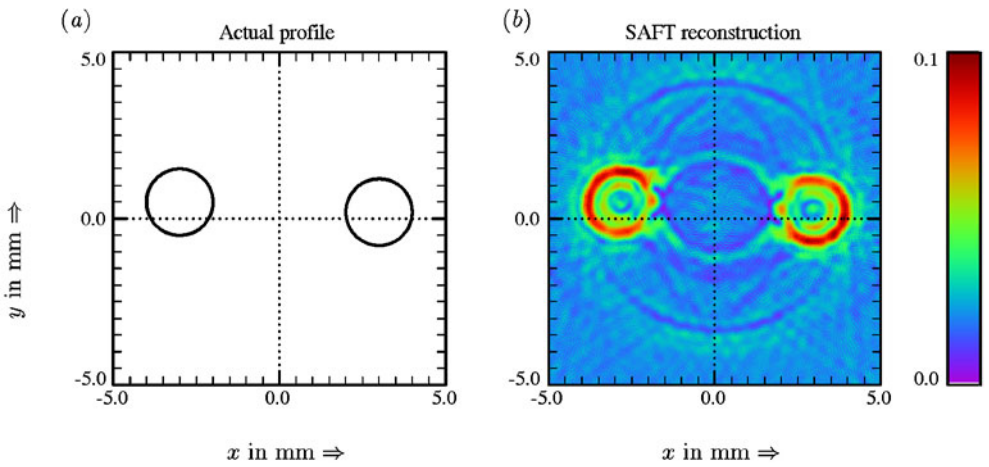

Figure 15. Images obtained for the multi-pulse–echo (multi-monostatic) data set; (*a*) Actual profile; (*b*) SAFT image.

The two air-filled scattering holes in the aluminium cylinder are placed closer to the x-axis as compared to the previous configuration. The exact profile is shown in figure 17(*a*). With 340 receiver positions for each of the 360 transmitter positions a considerable number of data is available, hence a data reduction is introduced considering only 36 transmitter positions placed 10° apart and 68 receiver positions placed 5° apart. The frequency band of the time domain

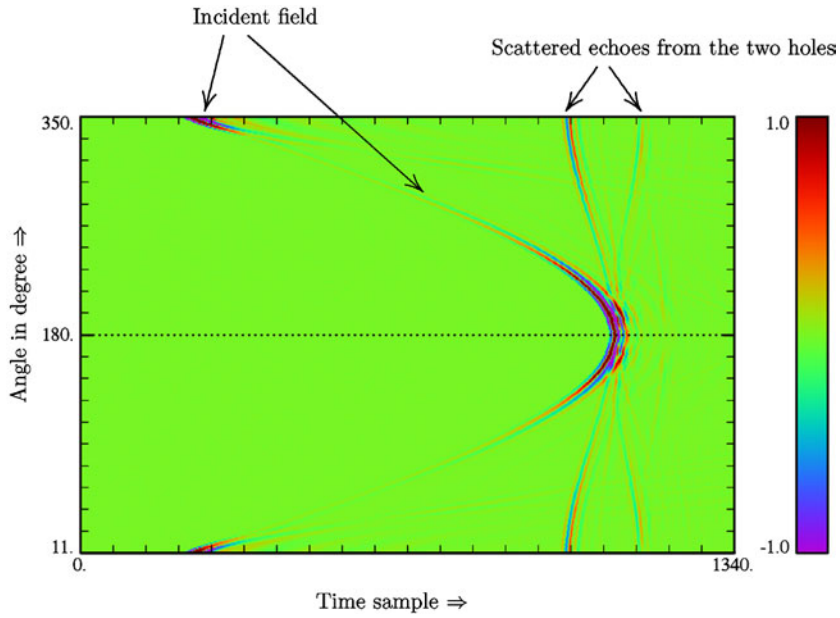

Figure 16. Measured ultrasonic multi-pitch–catch (multi-bistatic) time domain data set for the transmitter at 0°. The voltage output of the receiving transducer is plotted, which is normalized by the maximum value. The vertical axis shows the position angle of the receiving transducer in degrees. The horizontal axis shows the time samples for a total time of 16.75 μs. The sampling frequency is 80 MHz corresponding to a sampling distance of 12.5 ns.

data ranges from 3.5 to 7 MHz, hence 17 frequencies from 4.606 to 5.212 MHz with a spacing of 60.3 kHz are available, which are then subsequently used as the scattered field data as input to the algorithms. For the SAFT reconstruction shown in figure 17(*b*), we used the complete time domain data set, the CSIW and the ECSI algorithms were separately run for each of the 17 frequencies (a concurrent frequency (CF) or frequency hopping approach (Marklein *et al* 2001) is not performed). The best results were obtained for the CSIW at 4.545 MHz, plotted in figure 17(*c*), and for the ECSI at 4.303 MHz, as shown in figure 17(*d*). In both cases, the scatterer is assumed to be a perfect scatterer, whence the imaginary part of the contrast is computed and plotted in these images. The grid size is 64×64 over an area of 10 mm $\times$ 10 mm. It should be remembered that the wave speed is the propagation velocity of pressure waves in aluminium taken as $c_{\mathrm{P}} = 6297$ m s^{-1} resulting in a wavelength of 1.57 mm at 4 MHz yielding the radius of the holes to be $a = 1.27\,\lambda$ and the size of the domain V_D to be $6.37\lambda \times 6.37\lambda$.

Of the 17 frequencies mentioned before, the reconstruction was only possible for five frequencies with CSIW as well as ECSI. CSIW converged for 4.242, 4.545, 4.606, 4.909 and 4.970 MHz, while ECSI converged for 4.242, 4.303, 4.606, 4.667 and 5.030 MHz within the frequency range given above. A considerable amount of noise is present in each of these reconstructions, hence the results obtained at these five frequencies were added up to create a better contrast with less noise. This result is shown in figure 18(*c*) for the CSIW and in figure 18(*d*) for the ECSI reconstruction. We note that the CSIW reconstruction seems to have less noise than the ECSI reconstruction, and that there is a shadow that appears for the left hole for both the CSIW and the ECSI reconstructions. Even though the final residue of ECSI is less than that of CSIW for the same number of iterations, which was the main reason for its development, visual inspection does not confirm the superiority of the ECSI reconstruction.

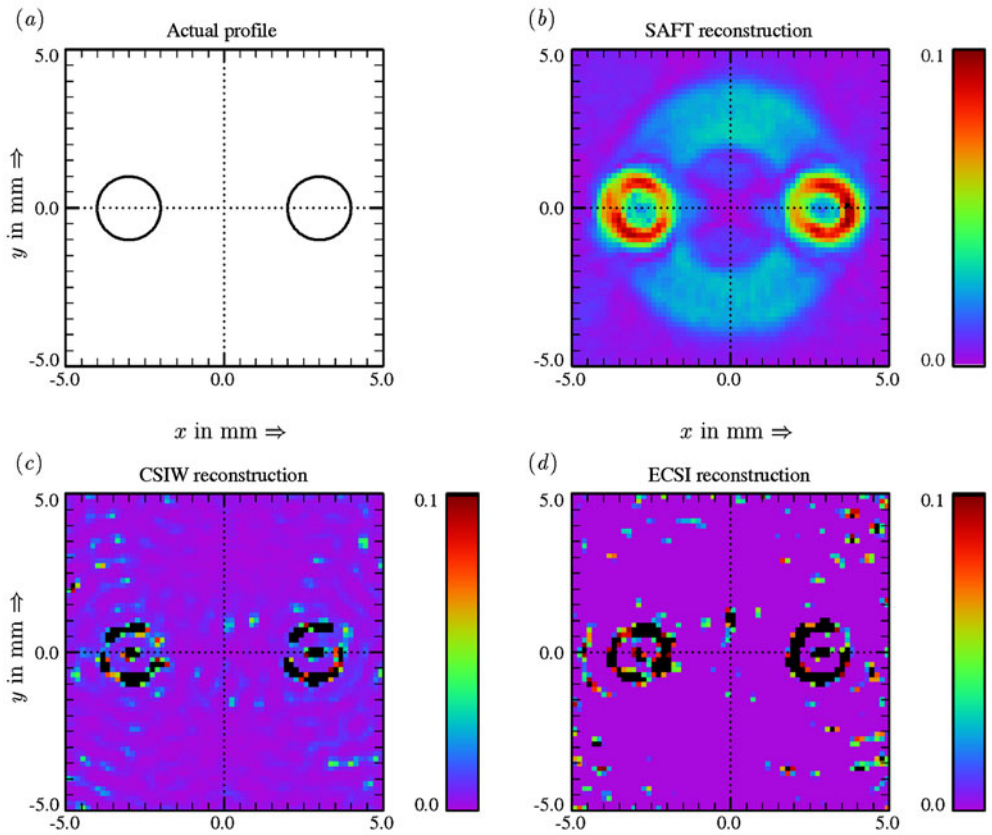

Figure 17. Images for the multi-pitch–catch (multi-bistatic) data set; (*a*) Actual profile; (*b*) SAFT image; (*c*) CSIW image for a single frequency of 4.545 MHz (256 iterations); (*d*) ECSI image for a single frequency of 4.303 MHz (256 iterations).

Further results for experimental electromagnetic scattering data can be found in Balasubramanian (2001) and Marklein *et al* (2001).

Presently, we are working on the extension of CSIW and ECSI to the vectorial and multi-mode cases (see also Pelekanos 1997, Pelekanos *et al* 2000, Arens 2001).

7. Conclusion

The paper demonstrates the considerable potential to extend and improve *the* ultrasonic imaging technique SAFT while consulting the mathematics of wavefield inversion, yet, in particular if the underlying effort is considered, the relatively simple and effective SAFT algorithm works surprisingly well.

Since SAFT is a widely accepted imaging tool in ultrasonic NDE it seems worthwhile to check its formal restrictions and assumptions—whether they could be overcome and whether they would outperform the standard and original SAFT algorithm.

- Being heuristically formulated, the inherent assumptions of SAFT inversion are not obvious *ab ovo*; yet the embedding of this algorithm within mathematical scalar wavefield inversion reveals that it is quantitatively related to linear time domain backpropagation

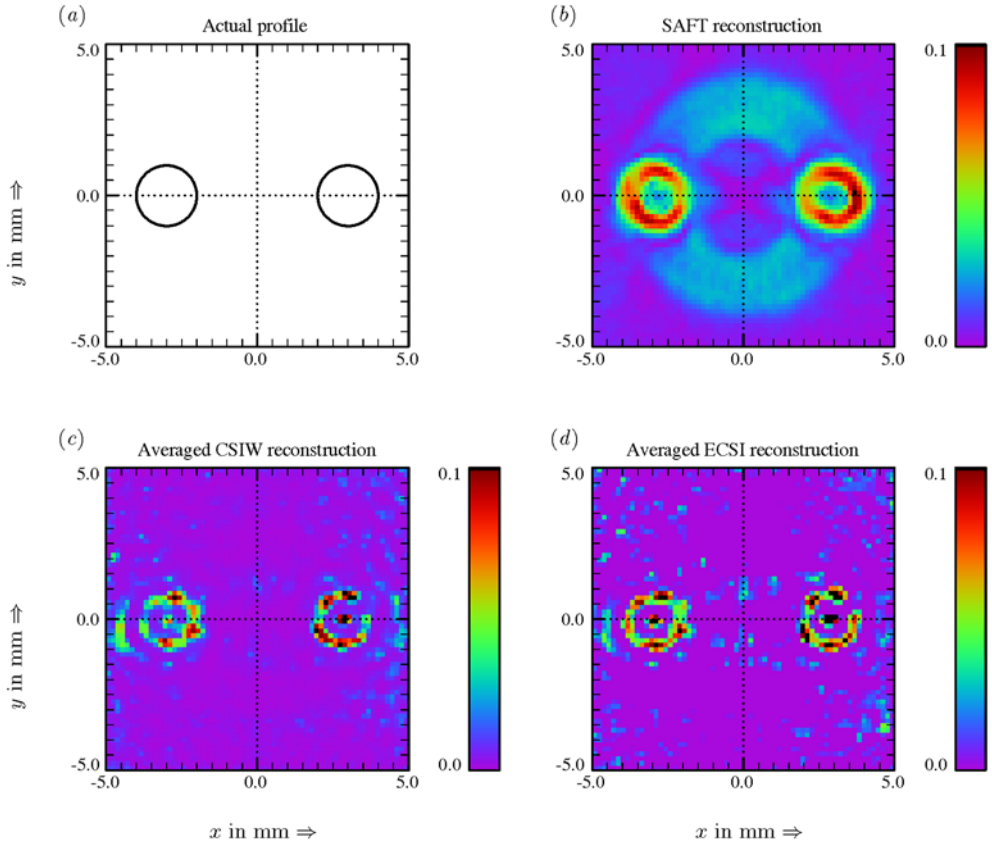

Figure 18. Reconstructions for the multi-pitch–catch (multi-bistatic) data set; (*a*) Actual profile; (*b*) SAFT image; (*c*) Averaged CSIW image obtained using five CSIW reconstructions for the data at frequencies 4.242, 4.545, 4.606, 4.909 and 4.970 MHz; (*d*) Averaged ECSI image obtained using five ECSI reconstructions for the data at frequencies 4.242, 4.303, 4.606, 4.667 and 5.030 MHz.

diffraction tomography. Due to the many articles on this subject, only references are given here.

- The linearization can be overcome by applying nonlinear inversion schemes. For the particular canonical NDE problem under consideration in this paper the result of SAFT still compares very well with well-tested nonlinear inversion schemes. Therefore, the question has to be answered, whether this continues to hold for more practically related test situations. Anyway, the problem is certainly the great number of very precise data to be recorded: the less sophisticated an algorithm is, the more robust it seems to be.
- The extension of SAFT to inhomogeneous and/or anisotropic background materials is a must for many applications, and this could be achieved along with the original 'theory' of SAFT. But, of course, more examples are needed.
- The scalar nature of SAFT can easily be overcome within the framework of linear vector wavefield inversion; this is true for electromagnetic as well as elastodynamic waves, yet, again, the problem seems to be the proper data acquisition: at the moment, utilization of synthetic data gives far better results than experimental data.

Final conclusion: not much remains to be done regarding the theoretical formulation of linear wavefield inversion, yet improvements with nonlinear inversion can certainly be made. Ockham's razor is simply: will it work in practice?

References

Abdullah H and Louis A K 1999 The approximate inverse for solving an inverse scattering problem for acoustic waves in an inhomogeneous medium *Inverse Problems* **15** 1213–29

Abubakar A 2000 *Three-Dimensional Nonlinear Inversion of Electrical Conductivity* (Delft: Delft University Press)

Abubakar A and van den Berg P M 2001 Total variation as a multiplicative constraint for solving inverse problems *IEEE Trans. Image Process.* **10** 1384–92

Arens T 2001 Linear sampling methods for 2D inverse elastic wave scattering *Inverse Problems* **17** 1445–64

Balasubramanian K 2001 Linear and nonlinear inverse scattering algorithms applied in 2D acoustics, electromagnetics and elastodynamics *Master Thesis* University of Kassel, Kassel

Bartsch T, Browman J, Cooper R K, Dehler M, Dohlus M, Ebeling F, Fischerauer A, Fischerauer G, Hahne P, Klatt R, Krawczyk F, Marx M, Pröpper T, Rodenz G, Rusthoi D, Schütt P, Steffen B, Weiland T and Wipf S 1990 Maxwell's grid equations *Frequenz* **44** 9–16

Belkebir K and Saillard M 2001 Special section: testing inversion algorithms against experimental data *Inverse Problems* **17** 1565–71

Bleistein N 1984 *Mathematical Methods of Wave Phenomena* (London: Academic)

Bleistein N, Cohen J K and Stockwell J R Jr 2001 *Mathematics of Multidimensional Seismic Imaging, Migration, and Inversion* (New York: Springer)

Bleistein N and Gray S H 2001 From the Hagedoorn imaging technique to Kirchhoff migration and inversion *Geophys. Prospect.* **49** 629–43

Brandfaß M 1996 *Inverse Beugungstheorie Elektromagnetischer Wellen: Algorithmen und Numerische Realisierung* (Aachen: Shaker)

Chew W C and Wang Y M 1990 Reconstructions of two-dimensional permittivity distribution using the distorted Born iterative method *IEEE Trans. Med. Imaging* **9** 218–25

Colton D and Kirsch A 1996 A simple method for solving inverse scattering problems in the resonance region *Inverse Problems* **12** 383–93

Colton D and Kress R 1998 *Inverse Acoustic and Electromagnetic Scattering Theory* (Berlin: Springer)

Colton D, Piana M and Potthast R 1997 A simple method using Morozov's discrepancy principle for solving inverse scattering problems *Inverse Problems* **13** 1477–93

Dändliker R and Weiss K 1970 Reconstruction of the threedimensional refractive index from scattered waves *Opt. Commun.* **1** 323

de Hoop A T 1995 *Handbook of Radiation and Scattering of Waves* (London: Academic)

Dikstra B J and Cameron N B 2002 Signal processing in qualified inspections of stainless steel welds: the SPIQNAR project *Proc. 8th European Conf. On Non-Destructive Testing (Barcelona/Spain, June 2002)*

Fellinger P, Marklein R, Langenberg K J and Klaholz S 1995 Numerical modeling of elastic wave propagation and scattering with EFIT—elastodynamic finite integration technique *Wave Motion* **21** 47–66

Fitch J P 1988 *Synthetic Aperture Radar* (New York: Springer)

Franchois A 1993 Contribution à la tomographie microonde: algorithmes de reconstruction quantitative et verifications experimentales *Thesis* Université de Paris–XI, Paris

Ganapathy S, Wu W S and Schmult B 1982 Analysis and design for a real-time system for nondestructive evaluation in the nuclear industry *Ultrasonics* **20** 249

Haak K F I 1999 *Multi-Frequency Nonlinear Profile Inversion Methods* (Delft: Delft University Press)

Habashy T M, Gross R W and Spies B R 1993 Beyond the Born and Rytov approximations—a nonlinear approach to electromagnetic scattering *J. Geophys. Res.* **98** 1759–75

Hagedoorn J G 1954 A process of seismic reflection interpretation *Geophys. Prospect.* **2** 85–127

Hannemann R 2002 *Modeling and Imaging of Elastodynamic Wave Fields in Inhomogeneous Anisotropic Media* (Berlin: dissertation.de-Verlag) http://www.dissertation.de

Helbig K 1994 *Foundations of Anisotropy for Exploration Seismics* (Oxford: Elsevier)

Inverse Problems 2001 *Inverse Problems* **17** 1565–701

Kirsch A 1998 Characterization of the shape of a scattering obstacle using the spectral data of the far field operator *Inverse Problems* **14** 1489–512

Kirsch A 1999 Factorization of the far-field operator for the inhomogeneous medium case and an application in inverse scattering theory *Inverse Problems* **15** 413–29

Kleinman R E and van den Berg P M 1992 A modified gradient method for two-dimensional problems in tomography *J. Comput. Appl. Math.* **42** 17–35

Kleinman R E and van den Berg P M 1994 Two-dimensional location and shape reconstruction *Radio Sci.* **29** 1157–69

Kleinman R E and van den Berg P M 1997 A contrast source inversion method *Inverse Problems* **13** 1607–20

Kostka J 2000 *Simulation und Inversion der Ausbreitung elastischer Wellen* (Aachen: Shaker)

Kostka J, Langenberg K J, Mayer K and Krause M 1998 Improved flaw imaging applying elastodynamic far–field Fourier inversion (EL-FT-SAFT) *Proc. 2nd Int. Conf. on Computer Methods and Inverse Problems in Nondestructive Testing and Diagnostics (Minsk, Oct. 1998)* pp 397–407

Langenberg K J 1987 Applied inverse problems for acoustic, electromagnetic and elastic wave scattering *Basic Methods for Tomography and Inverse Problems* ed P C Sabatier (Bristol: Hilger) pp 127–467

Langenberg K J 2002 Linear scalar inverse scattering *Scattering: Scattering and Inverse Scattering in Pure and Applied Science* vol 1, ed R Pike and P Sabatier (London: Academic) pp 121–41

Langenberg K J, Brandfaß M, Fellinger P, Gurke T and Kreutter T 1994 A unified theory of multidimensional electromagnetic vector inverse scattering within the Kirchhoff or Born approximation *Radar Target Imaging* ed W M Boerner and H Überall (Berlin: Springer) pp 113–51

Langenberg K J, Brandfaß M, Fritsch A and Potzkai B 1999a Linearized 3D electromagnetic vector wave inversion *Three-dimensional Electromagnetics* ed M Oristaglio and B Spies (Tulsa, OK: Society of Exploration Geophysicists)

Langenberg K J, Brandfaß M, Hannemann R, Hofmann C, Kaczorowski T, Kostka J, Marklein R, Mayer K and Pitsch A 1999b Inverse scattering with acoustic, electromagnetic, and elastic waves as applied in nondestructive evaluation *Wavefield Inversion* ed A Wirgin (Vienna: Springer) pp 59–118

Langenberg K J, Brandfaß M, Klaholz S, Marklein R, Mayer K, Pitsch A and Schneider R 1997 Applied inversion in nondestructive testing *Inverse Problems in Medical Imaging and Nondestructive Testing* ed A K Louis, H W Engl and W Rundell (Vienna: Springer)

Langenberg K J, Brandfaß M, Mayer K, Kreutter T, Brüll A, Fellinger P and Huo D 1993a Principles of microwave imaging and inverse scattering *EARSeL Adv. Remote Sens.* **2** 163–86

Langenberg K J, Fellinger P, Marklein R, Zanger P, Mayer K and Kreutter T 1993b Inverse methods and imaging *Evaluation of Materials and Structures by Quantitative Ultrasonics* ed J D Achenbach (Vienna: Springer) pp 317–98

Langenberg K J, Marklein R and Mayer K 2002 Applications to nondestructive testing with ultrasound *Scattering: Scattering and Inverse Scattering in Pure and Applied Science* vol 1, ed R Pike and P Sabatier (London: Academic) pp 594–617

Louis A K 1995 Approximate inverse for linear and some nonlinear problems *Inverse Problems* **11** 1211–12

Louis A K 1996 Approximate inverse for linear and some nonlinear problems *Inverse Problems* **12** 175–90

Maierhofer C, Borchardt K and Henschen J 1995 Application and optimization of impulse-radar for non-destructive testing in civil engineering *Proc. Int. Symp. on Non-Destructive Testing in Civil Engineering* vol 1, ed G Schickert and H Wiggenhauser (Berlin: DGZfP) pp 663–72

Marklein R 1997 *Numerische Verfahren zur Modellierung von akustischen, elektromagnetischen, elastischen und piezoelektrischen Wellenausbreitungsproblemen im Zeitbereich basierend auf der Finiten Integrationstechnik* (Aachen: Shaker)

Marklein R, Balasubramanian K, Qing A and Langenberg K J 2001 Linear and nonlinear iterative scalar inversion of multi-frequency multi-bistatic experimental electromagnetic scattering data *Inverse Problems* **17** 1597–610

Mayer K 1990 *Ultraschallabbildungsverfahren: Algorithmen, Methoden der Signalverarbeitung und Realisierung* (Kassel: Universität Gesamthochschule Kassel)

Mayer K, Marklein R, Langenberg K J and Kreutter T 1990 Three-dimensional imaging system based on Fourier transform synthetic aperture focusing technique *Ultrasonics* **28** 241–55

McGahan R V and Kleinman R E 1996 Special session on image reconstruction using real data *IEEE Antennas Propag. Mag.* **38** 39–59

McGahan R V and Kleinman R E 1997 Second annual special session on image reconstruction using real data *IEEE Antennas Propag. Mag.* **39** 7–32

McGahan R V and Kleinman R E 1999a The third annual special session on image reconstruction using real data: 1 *IEEE Antennas Propag. Mag.* **41** 34–51

McGahan R V and Kleinman R E 1999b The third annual special session on image reconstruction using real data: 2 *IEEE Antennas Propag. Mag.* **41** 20–40

Müller W and Schmitz V 2002 Synthetic aperture focusing technique—more than 20 years of experience *Inverse Problems* **18**

Pelekanos G 1997 Direct and inverse scattering by an elastic inclusion *PhD Thesis* University of Delaware, Delaware

Pelekanos G, Kleinman R E and van den Berg P M 2000 Inverse scattering in elasticity—a modified gradient approach *Wave Motion* **32** 57–65

Qing A 2001 Microwave imaging of parallel perfectly conducting cylinders with transverse electric scattering data *J. Electromagn. Waves Appl.* **15** 665–85

Qing A, Lee C K and Jen L 2001 Electromagnetic inverse scattering of two-dimensional perfectly conducting objects by real-coded genetic algorithm *IEEE Trans. Geosci. Remote Sens.* **39** 665–76

Roger A 1981 A Newton–Kantorovich algorithm applied to an electromagnetic inverse problem *IEEE Trans. Antennas Propag.* **29** 232–8

Snieder R 2002 General theory of elastic wave scattering *Scattering: Scattering and Inverse Scattering in Pure and Applied Science* ed R Pike and P Sabatier (London: Academic) pp 528–42

Spies M 1992 *Elastische Wellen in transversal-isotropen Medien: ebene Wellen, Gaußsche Wellenpakete, Greensche Funktionen, elastische Holographie* (Saarbrücken: Universität Saarbrücken)

Tijhuis A 1989 Born-type reconstruction of material parameters of an inhomogeneous lossy dielectric slab from reflected-field data *Wave Motion* **11** 151–73

van Bladel J 1996 *Singular Electromagnetic Fields and Sources* (Piscataway, NJ: IEEE)

van den Berg P M 1999 Reconstruction of media posed as an optimization problem *Wavefield Inversion* ed A Wirgin (Vienna: Springer) pp 191–240

van den Berg P M 2001 Non-linear scalar inverse scattering algorithms and applications *Scattering: Scattering and Inverse Scattering in Pure and Applied Sciences* ed E R Pike and P C Sabatier (London: Academic) pp 142–61

van den Berg P M, van Broeckhoven A L and Abubakar A 1999 Extended contrast source inversion *Inverse Problems* **15** 1325–44